

# Author response regarding the manuscript 'Coupling aerosol optics to the chemical transport model MATCH (v5.5.0) and aerosol dynamics module SALSA (v1)', to the short comment by A. Kerkweg

E. Andersson<sup>1</sup> and M. Kahnert<sup>1,2</sup>

<sup>1</sup>Chalmers University of Technology, Department of Earth and Space Sciences, SE-41296 Göteborg, Sverige

<sup>2</sup>Swedish Meteorological and Hydrological institute (SMHI), SE-60176 Norrköping, Sverige

March 24, 2016

Thank you for your comment and helping us full-fill the requirements of papers in GMD. We have included your comment in blue here in this document followed by our answer in black.

## 1 Short comment

Dear authors,

In my role as Executive editor of GMD, I would like to bring to your attention our Editorial version 1.1:

<http://www.geosci-model-dev.net/8/3487/2015/gmd-8-3487-2015.html> This highlights some requirements of papers published in GMD, which is also available on the GMD website in the "Manuscript Types" section:

[http://www.geoscientific-model-development.net/submission/manuscript\\_types.html](http://www.geoscientific-model-development.net/submission/manuscript_types.html)

In particular, please note that for your paper, the following requirement has not been met in the Discussions paper:

- Inclusion of Code and/or data availability sections is mandatory for all papers and should be located at the end of the article, after the conclusions, and before any appendices or acknowledgments.

You included the required information at the end of the conclusions sections. Please make the last sentence of your conclusions to an independent section with the title "Code and data availability" upon the revision of your article.

Yours, Astrid Kerkweg

Thank you for pointing this out, we have now added a section about the code availability after the conclusion section. The section is found on page 34 in the attached revised manuscript containing the differences between the previous version and the updated version of the manuscript.

# Coupling aerosol optics to the chemical transport model MATCH (v5.5.0) and aerosol **dynamics** microphysics module SALSA (v1)

E. Andersson<sup>1</sup> and M. Kahnert<sup>1,2</sup>

<sup>1</sup>Department of Earth and Space Sciences, Chalmers University of Technology, 41296 Gothenburg, Sweden

<sup>2</sup>Swedish Meteorological and Hydrological Institute, 60176 Norrköping, Sweden

*Correspondence to:* M. Kahnert (michael.kahnert@smhi.se)

**Abstract.** Modelling aerosol optical properties is a notoriously difficult task due to the particles' complex morphologies and compositions. Yet ~~aerosols~~ aerosol particles and their optical properties are important for ~~Earth-system-chemistry-climate~~ modelling and remote sensing applications. Operational optics models often make drastic and ~~non-realistic~~ non-realistic approximations regarding morphological properties, which can introduce errors. In this study a new ~~aerosol-optics~~ aerosol-optics model is implemented, in which more realistic morphologies and mixing states are assumed, especially for black carbon ~~aerosols~~ particles. The model includes both external and internal mixing of all chemical species, it treats ~~externally-mixed~~ externally-mixed black carbon as fractal aggregates, and it accounts for inhomogeneous internal mixing of black carbon by use of a novel “~~core-grey~~ shellcore-grey-shell” model. Simulated results of ~~radiative fluxes,~~ aerosol optical properties, such as aerosol optical depth, backscattering coefficients and ~~the~~ Ångström exponent ~~from,~~ as well as radiative fluxes computed with the new optics model are compared with results from ~~another model simulating an older optics-model version that treats all~~ particles as externally mixed homogeneous spheres. ~~To gauge the impact on the optical properties from the new optics model, the known and important effects from using aerosol dynamics serves~~ For comparison, we perform computations with two different model-versions, one that accounts for aerosol-microphysical processes, and another one that entirely neglects these processes. Since it is well understood that aerosol microphysics has a profound impact on aerosol mass- and number-concentrations, their size-distribution, and their size-dependent chemical composition (which, in turn, strongly impact their optical properties), these additional model-runs can serve as a reference against which we can gauge the significance of the morphological assumptions in the optics model. The results show that using a more detailed description of particle morphology and mixing states influences the optical properties to ~~the same~~

~~degree as aerosol dynamics.~~ a degree that is on the same order of magnitude as the corresponding effects of aerosol-microphysical processes. For instance, the aerosol optical depth computed with the two optics models differs over the optical spectrum by  $-25-18\%$ , while corresponding differences caused by the inclusion or omission of aerosol microphysics range between  $-50-37\%$ . The corresponding differences in the backscattering coefficient are  $-8-99\%$  and  $-47-28\%$ , respectively. This is an important finding suggesting that ~~over-simplified-simple~~ optics models coupled to a chemical transport model can introduce considerable errors; this can strongly ~~effect-affect~~ simulations of radiative fluxes in ~~Earth-system-chemistry-climate~~ models, and it can compromise the use of remote sensing observations of ~~aerosols-aerosol particles~~ in model evaluations and chemical data assimilation.

## 1 Introduction

~~Aerosol-optics~~ Aerosol-optics models are employed in large-scale chemical transport models (CTMs) in mainly two contexts, namely, in ~~Earth-system-climate-modelling-chemistry-climate-modelling~~ (CCM), and in conjunction with remote sensing observations. In ~~Earth-system-modelling-a-CCM~~ one couples a CTM to an atmosphere-ocean general circulation model (GCM). One purpose is to account for the dynamic effects of ~~aerosols-aerosol particles~~ on cloud microphysics. Another is to obtain a better description of the direct effect of ~~aerosols-aerosol particles~~ and radiatively active trace gases on the radiative balance. The ~~aerosol-optics-aerosol-optics~~ model provides a link that converts the aerosol fields delivered by the CTM to the aerosol optical properties that are required as input to the radiative transfer model, with which one computes the radiative energy budget. In remote sensing applications one is faced with the obstacle that the aerosol concentration fields computed with a CTM are not directly comparable to the radiometric quantities that are observed with remote sensing instruments. The ~~aerosol-optics-aerosol-optics~~ model provides the observation operator that maps the CTM output to radiometric variables that can be compared to satellite observations or satellite retrieval products. This allows us to either employ satellite observations for evaluating CTM model results, or to assimilate satellite data into a CTM-based air-quality forecasting system. It is clear that the ~~aerosol-optics-aerosol-optics~~ model has a pivotal role in these kinds of applications. It may constitute an additional source of error that could compromise the reliability of ~~Earth-system~~ climate-models CCMs, impair the reliability of CTM evaluations, or degrade chemical data assimilation results. It is, therefore, important to better understand this potential source of error, quantify its possible impact on model predictions of aerosol radiometric quantities, and assess the level of morphological detail that ~~is-required-in-aerosol-optics-might-be-required-in-aerosol-optics~~ models coupled to CTMs.

A main difficulty is that ~~aerosols-aerosol particles~~ in nature can have a high degree of morphological complexity. For instance, mineral dust particles can have irregular shape, small-scale surface roughness, and inhomogeneous mineralogical composition (e.g. Nousiainen, 2009). Black carbon

~~aerosols are fractal aggregates~~ particles suspended in air have fractal-aggregate shapes (e.g. Jones, 2006) that can be coated by weakly absorbing liquid-phase components that condense onto the aggregates as they age in the atmosphere (e.g. Adachi and Buseck, 2008). Volcanic ash particles are composed of crustal material in which multiple air vesicles may have been trapped during the generation of the particles. In ~~aerosol-optics~~ aerosol-optics models one has to make a choice what level of morphological detail is necessary and affordable. A detailed discussion of this question can be found in Kahnert et al. (2014).

65 In environmental modelling practical and computational constraints often force us to invoke drastically simplifying assumptions about aerosol morphology. For instance, one frequently computes aerosol optical properties based on the assumption that all chemical aerosol components are contained in separate particles (externally mixed), and that each such particle can be approximated as a homogeneous sphere. As pointed out in Kahnert (2008); Benedetti et al. (2009), this approach is 70 highly attractive from a practical point of view, because the aerosol optical observation operators, which map mixing ratios to radiometric properties, become linear functions of the mixing ratios of the different chemical species. A linearisation of the observation operator is a prerequisite for most of the commonly used ~~data-assimilation~~ data-assimilation methodologies, such as the variational method (e.g. Kahnert, 2008; Benedetti et al., 2009). However, such approximations can also intro- 75 duce substantial errors. In the ~~remote-sensing~~ remote-sensing community awareness for this problem has been growing over the past 1–2 decades. As a result, one has developed retrieval methods for desert dust ~~aerosols~~ aerosol particles that are based on spheroidal model particles (e.g. Dubovik et al., 2006), which can mimic the optical properties of mineral dust particles better than homogeneous spheres ~~Kahnert (2004); Nousiainen et al. (2006)~~ (Kahnert, 2004; Nousiainen et al., 2006). In 80 chemical data assimilation, the problem is still treated rather negligently. A few assimilation studies account for internal mixing (where several aerosol components can be contained within one particle) of different chemical components (e.g. Saide et al., 2013). But the particles are still assumed to be perfectly homogeneous spheres. To the best of our knowledge there are currently no aerosol optical observation operators in chemical transport models that take complex morphological properties of 85 ~~aerosols such as nonsphericity~~ aerosol particles such as non-sphericity or inhomogeneous internal structure into account.

This study describes the coupling of two different ~~aerosol-optics~~ aerosol-optics models to a regional CTM. One optics model is based on the simple external-mixture and homogeneous-sphere approximations. The second model takes both external and internal mixing of aerosol components into 90 account. Also, it employs morphologically more realistic models for black carbon ~~aerosols~~ particles. Although black carbon contributes, on average, only some 5 % to the mass mixing ratio of particulate matter over Europe, it can have a significant global radiative warming effect. Previous theoretical studies on the optical properties of ~~black-carbon aerosols~~ black-carbon particles suggest that the use of homogeneous sphere models can introduce substantial errors in the absorption cross section

95 and single scattering albedo of such particles (e.g. Kahnert, 2010a; Kahnert et al., 2013). Also, the largest mixing-state sensitivity in both regional and global radiative fluxes comes from black carbon according to Klingmüller et al. (2014).

The main goal of this study is to assess the impact of aerosol morphology and mixing state on radiometric quantities and radiative forcing ~~rates~~ simulated with a chemical transport model. To  
100 this end we compare the two optics models, and we gauge the significance of morphology by comparing the differences in the optics ~~models~~ model output to other sources of error. As a gauge we use the impact of including or omitting aerosol ~~dynamic~~ microphysical processes; this provides us with a reference which is generally agreed to have a significant effect on aerosol transport models (Andersson et al., 2015; Kokkola et al., 2008).

105 The CTM, its aerosol ~~dynamics~~ microphysic and mass transport ~~modules~~ set-ups, and the ~~aerosol optics model~~ aerosol-optics models are described in Sect. 2. There we also explain the methodology we employ for evaluation-comparison of the optics ~~model~~ models. In Sect. 3 we present and discuss computational results for selected cases and for several radiative and optical parameters. Concluding remarks are given in Sect. 4.

## 110 2 Model description and methods

### 2.1 General considerations and terminology

Aerosol particles typically originate from different emission sources, such as ~~seasalt~~ sea-salt particles coming from marine sources, wind-blown dust from dry land surfaces, volcanic ash from magmatic or phreatomagmatic eruptions, or black carbon produced during combustion of fossil fuel, biofuel,  
115 or biomass. During atmospheric transport particles from different sources can be mixed, resulting in heterogeneous aerosol populations consisting of particles of different morphologies, sizes, and chemical composition. A mixture in which different chemical species are contained in separate particles is referred to as an *external mixture*. On the other hand, aerosol dynamic processes, such as nucleation, condensation, and coagulation, give rise to the formation and growth of secondary particles from precursor gases, as well as to the condensation of precursor gases onto existing primary  
120 particles. These processes result in particles in which several chemical species are mixed with each other in one and the same particle. Such a population is referred to as an *internal mixture*. There are two types of internal mixtures. If, e.g., ~~hydrophillic~~ hydrophilic liquid-phase components mix with each other, one can obtain a *homogeneous internal mixture* of different chemical species. On  
125 the other hand, condensation of gas-phase species onto non-soluble primary particles, or cloud processing of ~~aerosols~~ aerosol particles can result in liquid-phase material coating a solid core of, e.g., mineral dust or black carbon. We refer to the latter as an *inhomogeneous internal mixture*. Aerosol populations in nature are often both externally and internally mixed, i.e., they contain particles that

are composed of a single chemical species as well as other particles that are composed of different  
130 chemical species, which can be homogeneously or inhomogeneously internally mixed.

Aerosol optical properties are strongly dependent on not only the size and chemical composition, but also on the mixing state, shape, and internal structure of particles. Therefore, before explaining the ~~aerosol-optics~~aerosol-optics model, we first need to briefly describe the kind of information that can be provided by the aerosol transport model. In particular, we need to understand the level of  
135 detail with which the size distribution, size-dependent chemical composition, and the mixing state of the ~~aerosols~~aerosol particles can be computed in a large-scale model.

## 2.2 Aerosol transport modelling with MATCH

As a regional model we employ the Multiple-scale Atmospheric Transport and CHemistry modelling system (MATCH)~~Andersson et al. (2007)~~, an offline Eulerian model developed by the Swedish  
140 Meteorological and Hydrological Institute (Andersson et al., 2007). For this study we have set up the MATCH model over the European domain with a  $0.4 \times 0.4^\circ$  horizontal resolution and a rotated latitude-longitude grid, covering about  $34^\circ$  longitude and  $42^\circ$  latitude. The model has 40 vertical  $\eta$  layers with varying thickness depending on the topography, and it extends up to about 13 hPa. The meteorological input comes from the numerical weather-prediction model HIRLAM (High-Resolution  
145 Limited Area Model) (Unden et al., 2002).

The MATCH model allows us to choose between two aerosol model versions, a simpler ~~mass transport~~mass-transport model, and a more sophisticated aerosol dynamic transport model.

### 2.2.1 Mass transport model

A simple version of the CTM MATCH, which we refer to as the “~~mass-transport~~mass-transport  
150 model”, neglects all aerosol dynamic processes. It contains a photochemistry model that computes mass concentrations of secondary inorganic aerosols (SIA), which are formed from precursor gases. The SIA fraction of aerosol particles consists of ammonium sulphate ( $(\text{NH}_4)_2\text{SO}_4$ ), ammonium nitrate ( $\text{NH}_4\text{NO}_3$ ), other particulate sulphates ( $\text{PSO}_x$ ), and other particulate nitrates ( $\text{PNO}_x$ ). The mass transport model further contains a ~~seasalt~~sea-salt module that computes NaCl emissions based on the  
155 parametrisations described in Mårtensson et al. (2003); Monahan et al. (1986). ~~It~~More details on the MATCH photochemistry model can be found in Robertson et al. (1999); Andersson et al. (2007); the MATCH sea-salt model is described in Foltescu et al. (2005). The mass transport model also contains a simple wind-blown dust model and a module for transport of primary particulate matter (PPM), i.e., ~~aerosols other than seasalt and windblown~~aerosol particles other than sea-salt and  
160 wind-blown dust that are emitted as particles, rather than being formed from gas precursors. The size bins in the PPM model are flexible. In the current model set-up the ~~sea-salt~~sea-salt and PPM models were run for four size bins as shown in Table ~~??~~1. We used gridded EMEP PPM emission data for the year 2007 ~~, and, based on those and on Kupiainen and Klimont (2004, 2007), we~~

**Table 1.** Size bins (characterised by the radius  $r$ ) and chemical species in the MATCH mass transport model (Andersson et al., 2007). The labels “p” and “s” refer to primary emitted particles and secondary particles generated from gas precursors.

size bin	$r$ (nm)	OC	BC	<del>wind-blown</del> Dust	other PPM	NaCl	(NH <sub>4</sub> ) <sub>2</sub> SO <sub>4</sub>	NH <sub>4</sub> NO <sub>3</sub>	other PSO <sub>x</sub>	other PNO <sub>x</sub>
1	10–50	p	p		p	p	s	s	s	s
2	50–500	p	p		p	p	s	s	s	s
3	500–1250					p	s	s	s	s
4	1250–5000	p	p	p	p	p	s	s	s	s

generated gridded emission data for black carbon in conjunction with black-carbon (BC), organic carbon and organic-carbon (OC), and all other PPM. (Here, OC refers to the mass of all organic matter, not just the mass of carbon atoms in organic compounds.) The primary particle emission data by Kupiainen and Klimont (2004, 2007). The latter provide BC and OC emissions per country and emission sector. We distributed these among the grid cells in the model domain according to the EMEP PPM gridded emissions. Thus, the BC and OC emissions vary among grid cells in accordance with the EMEP PPM emissions, while the sum of all BC and OC emissions over all grid cells per country and emission sector agrees with the corresponding BC and OC emissions, respectively, reported in Kupiainen and Klimont (2004, 2007). The remaining emissions (PPM-BC-OC) in each grid cell are interpreted as dust particles. The primary-particle emissions are distributed among the four size classes size bins; during atmospheric transport they remain chemically and dynamically inert in the model. Thus no chemical transformation, mixing processes with other compounds, or other size transformation size-transformation processes are included in the model. The SIA components are given as total mass concentrations without any information about their size distribution. In the optics model a fixed size distribution is assumed to assign the total SIA mass to the four size bins. Water adsorption by particles is computed in the optics model as described in Sect. 2.3.1. More details on the MATCH photochemistry model can be found in Robertson et al. (1999); Andersson et al. (2007). The MATCH seasalt model is described in Foltescu et al. (2005).

### 2.2.2 Aerosol dynamics model microphysics module - SALSA

A more realistic description of particles can be achieved by accounting for aerosol dynamic-microphysical processes. To this end the Sectional Aerosol module for Large Scale Applications (SALSA) (Kokkola et al., 2008) has recently been coupled to the MATCH photochemistry model (Andersson et al., 2015). This model tracks mass concentrations of different species per size bin, and particle number concentrations. Thus, it provides size-dependent composition and mixing state of aerosol particles. The description of PNO<sub>x</sub>, wind-blown dust, and secondary organic aerosols (SOA) is still under development in an early development stage in MATCH-SALSA. A simplified In the current version,

190 ~~PNO<sub>x</sub> description has been included in the model version employed here, while wind-blown is~~  
simply computed according to the same photochemistry-scheme as in the mass-transport model, and  
the PNO<sub>x</sub> mass is assigned to size bin 15 (see Tab. 2). Wind-blown dust and SOA are absent. ~~The~~  
~~number and range of size bins is flexible in SALSA. Table ?? in the present model version. The size~~  
distributions for the emitted particles can be found in table 4 and figure 6 of Andersson et al. (2013).

195

Table 2 shows the current model set-up ~~with the number and range of the size bins.~~

As is evident from the this table, MATCH-SALSA  
accounts for both internally and externally mixed aerosols-aerosol particles. In total, there are  
20 different size bins in MATCH-SALSA, each one of them representing a particle size range  
200 (volume-equivalent radius,  $r$ ), mixing state, and composition. Some size bins have the same size  
range, but different mixing states and/or compositions. For instance, size bins 12, 15, and 18 de-  
scribe the same size range (~~350-873~~350-873 nm), but different internal mixtures of various species.  
Similarly, bins 4 and 8 have the same size range (25-49 nm), but one describes an internal mixture,  
the other an external mixture of aerosol species.

205 ~~Note that water is not directly calculated as a prognostic variable in MATCH-SALSA. Rather,~~  
~~it is a diagnostic variable computed in the MATCH-optics model as explained in Sect. 2.3.2. The~~  
~~table merely indicates which size bins are assumed in the optics model to be internally mixed~~  
~~with adsorbed water. A more detailed description of the MATCH-SALSA model can be found in~~  
~~Andersson et al. (2015).~~

### 210 **2.3 Aerosol optics modelling**

As in the mass-transport model, "other PPM", i.e. primary particles other than BC and OC, are  
interpreted as dust particles. Note that water is not directly calculated as a prognostic variable  
in MATCH-SALSA. Rather, it is a diagnostic variable computed in the MATCH-optics model as  
explained in Sect. 2.3.2. The table merely indicates which size bins are assumed in the optics model  
215 to be internally mixed with adsorbed water. A more detailed description of the MATCH-SALSA  
model can be found in Andersson et al. (2015).

~~Aerosol optics~~

### 2.3 Aerosol optics modelling

Aerosol-optics models coupled to a CTM have to make consistent use of the information provided  
220 by the CTM, while invoking assumptions on optically relevant parameters that are not provided by  
the CTM. The parameters that influence the particles' optical properties are

- the aerosol size distribution;
- the refractive index of the materials of which the ~~aerosols~~aerosol particles are composed;



**Table 2.** Size bins and chemical species in the MATCH-SALSA aerosol ~~dynamic-microphysical~~ transport model. An “x” marks that the species is present in a particular size bin.

size bin	$r$ (nm)	mixing state	OC	BC	PPM	NaCl	PSO <sub>x</sub>	PNO <sub>x</sub>	PNH <sub>x</sub>
1	1.5–3.8	internal	x				x		x
2	3.8–9.8	internal	x				x		x
3	9.8–25	internal	x				x		x
4	25–49	internal+H <sub>2</sub> O	x	x	x	x	x		x
5	49–96	internal+H <sub>2</sub> O	x	x	x	x	x		x
6	96–187	internal+H <sub>2</sub> O	x	x	x	x	x		x
7	187–350	internal+H <sub>2</sub> O	x	x	x	x	x		x
8	25–49	external	x	x			x		x
9	49–96	external	x	x			x		x
10	96–187	external	x	x			x		x
11	187–350	external	x	x	x		x		x
12	350–873	NaCl+H <sub>2</sub> O				x			
13	873–2090	NaCl+H <sub>2</sub> O				x			
14	2090–5000	NaCl+H <sub>2</sub> O				x			
15	350–873	internal+H <sub>2</sub> O	x	x	x		x	x	x
16	873–2090	internal+H <sub>2</sub> O	x		x		x		x
17	2090–5000	internal+H <sub>2</sub> O	x		x		x		x
18	350–873	internal+H <sub>2</sub> O			x		x		x
19	873–2090	internal+H <sub>2</sub> O			x		x		x
20	2090–5000	internal+H <sub>2</sub> O			x		x		x

– the morphology of the particles.

225 *Morphology* refers to both the overall shape of the particle, and, in case of inhomogeneously mixed particles, the variation of the refractive index inside the particle.

The information provided by the CTM depends on the level of detail in the process descriptions. In the MATCH mass transport model, we have size information for the primary particles, but only the total mass for secondary inorganic aerosols. Thus we have to invoke assumptions about the size  
230 distribution of these particles. The MATCH optics models in conjunction with the MATCH mass transport model assume that 10 % of the SIA aerosol mass are in the smallest size ~~class-bin~~ (see Table ~~??1~~), 60 % in the second, 20 % in the third, and 10 % in the fourth size ~~classbin~~. Also, the mass transport model lacks any information about the mixing state of the particles. We therefore  
235 have to invoke appropriate assumptions on whether the ~~aerosols-aerosol particles~~ are externally or internally mixed. Both the mass transport model and MATCH-SALSA lack information on whether the internally mixed particles are homogeneous or inhomogeneous. Also, neither model provides any information on the shape of the particles. The refractive ~~index-of-the-different-chemical-components~~  
~~indices of each chemical component~~ in the aerosol phase and their spectral variation ~~is-given-in-are~~

listed in Appendix D. They can also be found in Fig. 4 of in Kahnert (2010a). That reference also  
240 contains detailed information about the different literature sources from which the refractive indices  
are taken.

### 2.3.1 Optics model for externally mixed aerosols/aerosol particles

The simplest conceivable optics model assumes that all particles are homogeneous spheres, and  
that all chemical species are each in separate particles, i.e., externally mixed. As explained in  
245 Kahnert (2008) (Kahnert, 2008), the external-mixture assumption results in a linear relation between  
the mass mixing ratios and the optical properties. Owing to the linearity, this model is particularly  
attractive for data assimilation applications (e.g. Benedetti et al., 2009), which require linearised  
observation operators. However, this is also the crudest possible optics model, as it neglects both the  
effect of internal mixing and of particle morphology on optical properties.

250 The external-mixture model is implemented in the MATCH mass transport model, where it is pri-  
marily being used in the MATCH 3DVAR data assimilation system Kahnert (2008) (Kahnert, 2008).  
Optical properties are pre-computed for twelve wavelength bands ranging from the UV-C to the mid-  
IR. Dust and black carbon are assumed to be hydrophobic, while sea salt, OC, and SIA components  
can each mix internally with water. The water volume fraction depends on temperature and humidity;  
255 it is computed by use of the parametrisation given in Gerber (1985), which computes the particle's  
wet-radius as a function of dry-radius, relative humidity, and temperature. The aerosol/water mix-  
ture is assumed to be homogeneous. The dielectric properties of a homogeneous mixture of two  
or more components are described by a complex effective refractive index  $m_{\text{eff}}$ , which is usually  
computed by effective medium theory (EMT) (although chemical transport modellers often use sim-  
260 ple volume mixing rules, most likely because EMTs are not commonly known in that field). We  
use Bruggemann's EMT (Bruggemann, 1935). More information of EMT is given in Appendix C.  
Optical properties are pre-computed for eleven water volume fractions between 0 and 0.98; for in-  
termediate volume fractions the optical properties are linearly interpolated. The optical properties  
contained in the database are the extinction cross section  $C_{\text{ext}}$ , the scattering cross section  $C_{\text{sca}}$ , the  
265 value of the phase function in the exact backscattering direction  $p(180^\circ)$ , and the asymmetry param-  
eter  $g$ .

As explained in Kahnert (2008), size-averaged optical properties are pre-computed by averaging  
over a log-normal size distribution  $n_i(r) = N_i / (\sqrt{2\pi} r \ln \sigma_i) \exp[-\ln^2(r/r_i) / (2 \ln^2 \sigma_i)]$   
 $n_i(r) = N_i^0 / (\sqrt{2\pi} r \ln \sigma_i) \exp[-\ln^2(r/R_i) / (2 \ln^2 \sigma_i)]$  for each size class-bin  $i$ , where  $N_i$  represents  
270  $N_i^0$  relates to the number density of particles in size bin  $i$ ,  $r$  denotes the particle radius,  $r_1 = 0.022$   
 $R_1 = 0.022 \mu\text{m}$ ,  $r_2 = 0.158 R_2 = 0.158 \mu\text{m}$ ,  $r_3 = 0.791 R_3 = 0.791 \mu\text{m}$ ,  $r_4 = 2.5 R_4 = 2.5 \mu\text{m}$  are the  
geometric mean radii in each size mode, and the variances geometric standard deviation  $\sigma_1 = \sigma_3 =$   
 $\sigma_4 = 1.8$ ,  $\sigma_2 = 1.5$  are based on measurements in Neusüß et al. (2002). The volume per size bin  
can be obtained by integrating  $(4/3)\pi r^3 n_i(r)$  over the  $i$ th size bin interval; this can be used for

275 ~~converting~~ Appendix A provides detailed explanations of how to convert mass mixing ratios into  
number densities in each size bin, which, in turn, allows us to compute radiative properties computed  
in the model into particle number densities, how these are used in computing size-averaged optical  
properties, and how to obtain radiometric properties of the atmosphere, such as aerosol optical depth  
(AOD), ~~single-scattering albedo (SSA), asymmetry parameter  $g$ , and or~~ backscattering coefficient  
280  $\beta_{\text{bak}}$  in each atmospheric grid cell in MATCH—see Kahnert (2008) for details, from the particles’  
optical properties and from the MATCH aerosol fields.

### 2.3.2 Optics model for ~~aerosols~~ aerosol particles of different mixing states

The new MATCH-optics model accounts for both internally and externally mixed ~~aerosols~~ aerosol  
particles, and it contains both homogeneously and inhomogeneously mixed ~~aerosols~~ aerosol particles.  
285 Different shapes and morphologies are assumed for different types of particles.

1. Pure, externally mixed black carbon ~~aerosols~~ particles are assumed to have a fractal aggregate  
morphology as shown in Fig. 1. The fractal morphology can be described by the statistical  
scaling law  $N_s = k_0(R_g/a)^{D_f}$ , where  $N_s$  denotes the number of spherical monomers in the  
aggregate,  $D_f$  and  $k_0$  are the fractal dimension and fractal prefactor,  $a$  is the monomer radius,  
290 and  $R_g = \sqrt{\sum_{n=1}^{N_s} r_n^2 / N_s}$  is the radius of gyration, where  $r_n$  describes the distance of the  $n$ th  
monomer from the aggregate’s centre of mass. We use  $D_f = 1.8$ ,  $k_0 = 1.3$ , which is based on  
the review in Bond and Bergstrom (2006). Although in the atmosphere black carbon aggre-  
gates may also have higher fractal dimensions (e.g. Adachi et al., 2007; [Chakrabarty et al., 2014](#);  
[China et al., 2014](#)), assuming a ~~lower~~ fractal dimension around 1.8 yields ~~mass-absorption~~  
295 ~~cross-sections~~ mass-absorption cross sections at 550 nm wavelength that lie closer to ex-  
perimental data, as was shown in Kahnert and Devasthale (2011). The monomer radius ~~was~~  
~~can vary within a range of 10-25 nm (Bond and Bergstrom, 2006). Here it is~~ assumed to be  
 $a = 25$  nm. This is consistent with field observations (Adachi and Buseck, 2008); also, it was  
shown (Kahnert, 2010b) that this choice of monomer radius in light scattering computations  
300 yields results for the single-scattering albedo of black carbon aggregates consistent with ob-  
servations ([Bond and Bergstrom, 2006](#)).

The ~~calculation~~ calculations in Kahnert and Devasthale (2011) were limited to aggregates up  
to  $N_s = 600$ . In order to cover the size range of externally mixed black carbon in SALSA  
we had to extend these calculations to aggregate sizes up to  $N_s = 2744$ , which corresponds to  
305 a volume-equivalent radius of  $R_V = 350$  nm (compare with Table [???](#)). We used the multiple-  
sphere T-matrix code (Mackowski and Mishchenko, 2011), which is based on the numerically  
exact superposition T-matrix method for solving Maxwell’s equations. Figure 2 shows some of  
the computed black carbon optical properties as a function of ~~partiele-size~~ volume-equivalent  
particle radius and wavelength. All optical properties are averaged over particle orientations,  
310 ~~where the orientation-averaging is performed analytically (Khlebstov, 1992)~~. The absorption

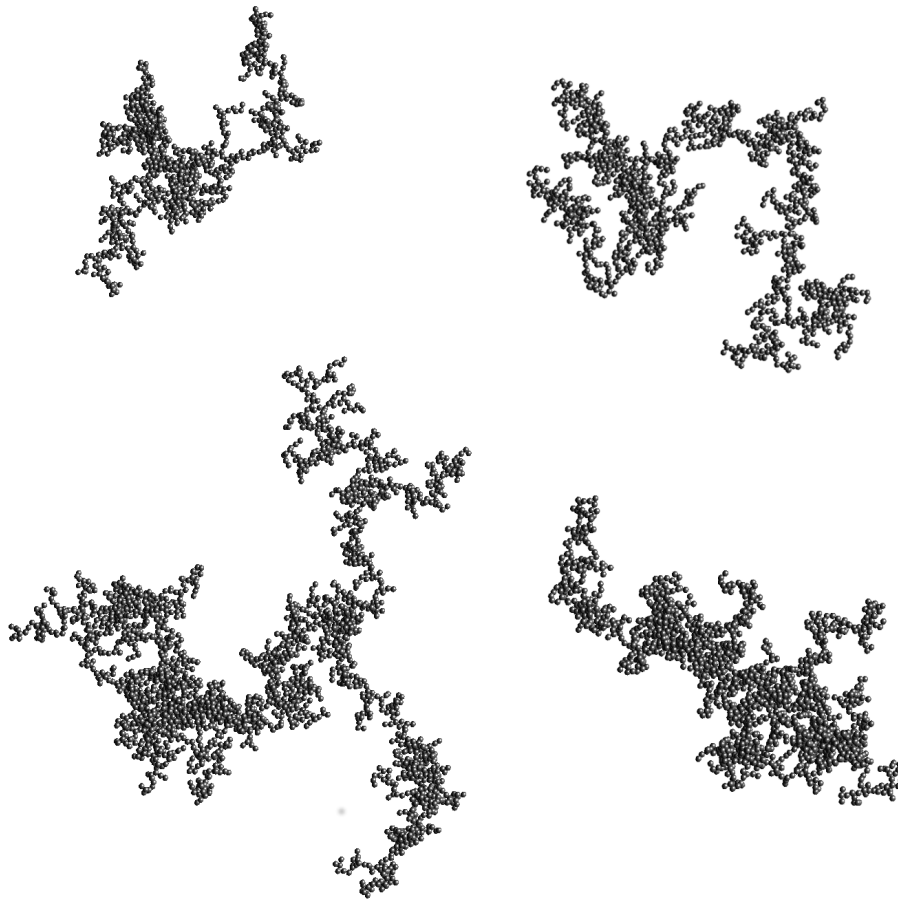


**Figure 1.** Examples of fractal aggregate model particles for computing optical properties of externally mixed black carbon. The aggregates consist of 1000, 1500, 2000, and 2744 monomers (in clockwise order, starting from upper left).

cross section  $C_{\text{abs}}$  shows the characteristic decline  $\sim 1/\lambda$  at long wavelengths, where the refractive index of black carbon is changing only slowly (Chang and Charalampopoulos, 1990). Also,  $C_{\text{abs}}$  increases with particle size. For small particle sizes this increase goes as  $\sim R_V^3$ , which is typical for the Rayleigh scattering regime (Mishchenko et al., 2002).

- 315      2. Black carbon ~~aerosols~~ particles that are internally mixed with other aerosol components are morphologically very complex. It is technically beyond the reach of our present capabilities to build an ~~aerosol-optics~~ aerosol-optics database with the use of morphologically realistic model particles. However, it is possible to employ realistic model particles in reference computations for some selected cases. This has recently been done in ~~Kahnert et al. (2013)~~. In that study ~~different studies~~ Kahnert et al. (2013); Scarnato et al. (2013, 2015). In the study by ~~Kahnert et al. (2013)~~, optical properties of encapsulated aggregate model particles, such as the one shown in Fig. 3 (left), were computed in the ~~size range~~ from range of 100–500 nm
- 320

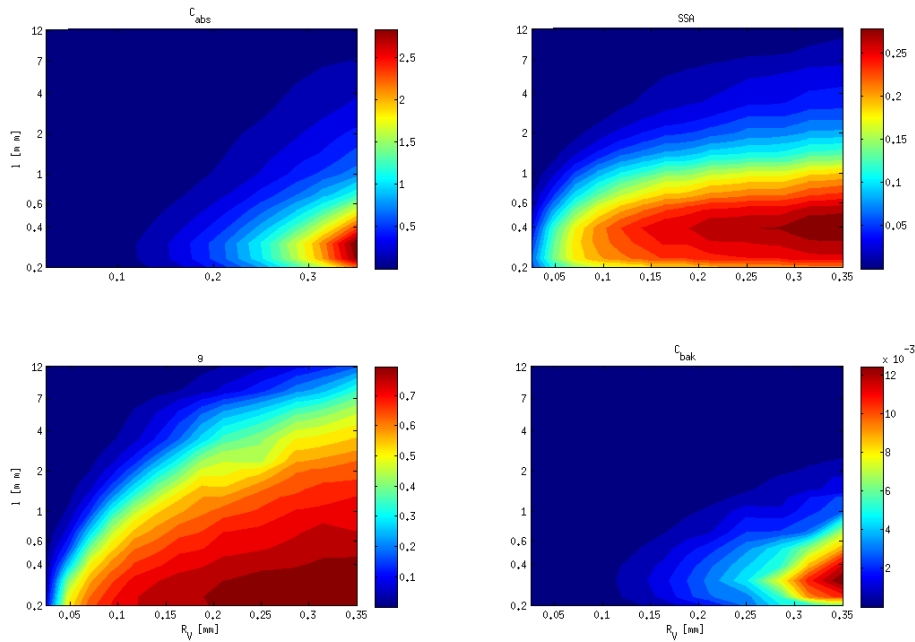


**Figure 2.** Absorption cross section  $C_{\text{abs}}$  (upper left), single-scattering albedo SSA (upper right), asymmetry parameter  $g$  (bottom left), and backscattering cross section  $C_{\text{bak}}$  (bottom right) of black carbon aggregates as a function of volume-equivalent radius  $R_V$  and wavelength  $\lambda$ .

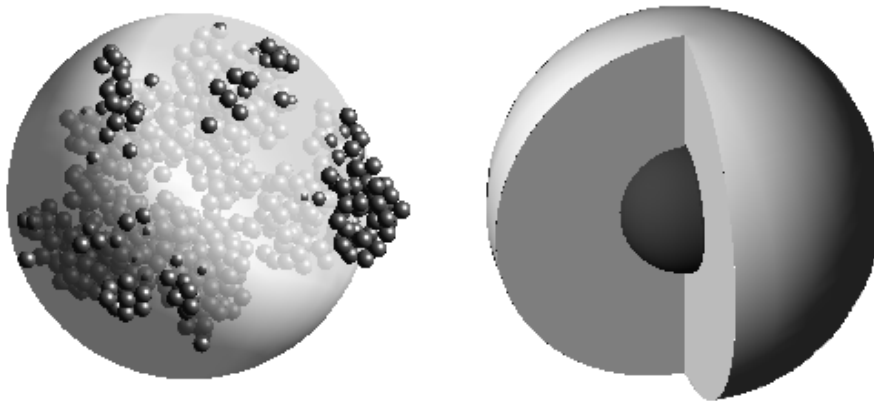


**Figure 3.** Morphologically realistic encapsulated aggregate model for internally mixed black carbon (left), and core-greyscale model (right).

([volume-equivalent radius](#)), for different black carbon volume fractions, and for wavelengths from the UV-C to the mid-IR. The morphological parameters characterising these model particles were based on field observations (Adachi and Buseck, 2008); the coating material was sulphate. The computations were performed with the discrete dipole approximation (Yurkin and Hoekstra, 2007).

In Kahnert et al. (2013) the computational results were compared to those obtained with simple model particles, such as ~~externally-mixed~~externally-mixed homogeneous spheres, ~~internally-mixed~~internally-mixed homogeneous spheres, and concentric core-shell particles with a carbon core and a sulphate shell. The analysis revealed which morphological properties of the encapsulated aggregate particles had the dominant impact on the optical properties. There are two important properties: (1) the amount of carbon mass that interacts with the electromagnetic field has a major impact on the absorption cross section  $C_{\text{abs}}$ . In a core-shell model as well as in a model based on externally mixed homogeneous spheres, all of the black carbon is concentrated in a single sphere. Owing to absorption of the electromagnetic field does not penetrate deeply into this sphere. Hence much of the carbon mass is shielded from interacting with the field, resulting in an underestimation of  $C_{\text{abs}}$  compared to the encapsulated aggregates, in which a much larger fraction of the carbon mass can contribute to the absorption of electromagnetic energy. By contrast, in a homogeneous ~~internal-mixture~~internal-mixture model the black carbon is distributed evenly throughout the sulphate host, which allows too much of the carbon mass to interact with the field. This results in an overestimation of  $C_{\text{abs}}$ . (2) Compared to a ~~bare-black~~bare-black carbon aggregate, a coated aggregate has a larger geometric cross section. Hence more light is intercepted by an ~~internally-mixed~~internally-mixed particle and focused onto the black carbon inclusion, thus enhancing  $C_{\text{abs}}$ . This effect is neglected in the ~~external-mixture~~external-mixture model, resulting in an underestimation of  $C_{\text{abs}}$ .

~~One~~ Note that in earlier studies (e.g. Jacobson (2000)) it was often tacitly assumed that a core-shell model would give the most accurate estimates of the aerosol optical properties, owing to its morphological similarity to encapsulated black-carbon particles. However, the results in Kahnert et al. (2013) have clearly shown the shortcomings of the conventional core-shell model. But once we understand which morphological properties are most essential, and which ones make a minor contribution to the optical properties, we can devise model particles that account for the most important morphological effects, yet are sufficiently simple for computing a look-up table for large-scale modelling. It was proposed in Kahnert et al. (2013) to use a core-shell model (hence accounting for the coating effect) in which only part of the carbon mass is contained in the core, and the remaining part is homogeneously mixed with the shell. The model particle is illustrated in Fig. 3 (right). The ~~core-shell-partitioning-fraction~~core-shell-partitioning-fraction  $f_c$  of the carbon mass located in the core is a free parameter, with which one can interpolate between the two extreme models of the homogeneous mixture ( $f_c = 0$ , all carbon mass mixed with the shell) and the regular core-shell model ( $f_c = 1$ , all carbon mass in the core). This model has been referred to as the concentric core-grey-shell (CGS) model. The tuning of the free parameter  $f_c$  in the model was done to fit the reference model of encapsulated aggregates as described in Kahnert et al. (2013). It was found that  $f_c$  is independent of particle size,

**Table 3.** Core fraction  $f_c$  in the core-grey-shell model as a function of wavelength  $\lambda$ .

$\lambda$ [ $\mu\text{m}$ ]	<u>0.2000</u>	<u>0.2316</u>	<u>0.3040</u>	<u>0.3400</u>	<u>0.3550</u>	<u>0.3800</u>	<u>0.3932</u>
$f_c$	<u>0.7</u>	<u>0.7</u>	<u>0.7</u>	<u>0.7</u>	<u>0.7</u>	<u>0.6</u>	<u>0.6</u>
$\lambda$ [ $\mu\text{m}$ ]	<u>0.4400</u>	<u>0.5000</u>	<u>0.5320</u>	<u>0.5332</u>	<u>0.6750</u>	<u>0.7016</u>	<u>0.8700</u>
$f_c$	<u>0.6</u>	<u>0.5</u>	<u>0.5</u>	<u>0.5</u>	<u>0.5</u>	<u>0.5</u>	<u>0.2</u>
$\lambda$ [ $\mu\text{m}$ ]	<u>1.0101</u>	<u>1.0200</u>	<u>1.064</u>	<u>1.2705</u>	<u>1.4625</u>	<u>1.7840</u>	<u>2.0460</u>
$f_c$	<u>0.1</u>	<u>0.1</u>	<u>0.1</u>	<u>0.1</u>	<u>0.1</u>	<u>0.1</u>	<u>0.1</u>
$\lambda$ [ $\mu\text{m}$ ]	<u>2.3250</u>	<u>2.7885</u>	<u>3.4615</u>	<u>3.5000</u>	<u>8.0205</u>	<u>10.600</u>	<u>12.195</u>
$f_c$	<u>0.1</u>	<u>0.1</u>	<u>0.1</u>	<u>0.1</u>	<u>0.1</u>	<u>0.1</u>	<u>0.1</u>

black-carbon volume fraction, and of the optical property one wants to fit. However,  $f_c$  does depend on the wavelength of light.

The CGS model has been employed in generating the new MATCH-optics look-up table. The shell material can be any mixture of water-soluble components. We use the same values of  $f_c$  as those determined in Kahnert et al. (2013). Its dependence on wavelength is given in Table 3.

3. In the mass transport model, we assume that all SIA components and all sea salt is internally mixed. We further assume that in size classes-bins 1–4, 0, 70, 70, and 100 %, respectively, of the black carbon, 0, 70, 70, and 70 % of the organic carbon, and 0, 1.3, 1.3, and 1.3 % of the dust are internally mixed; the remaining BC, OC, and dust mass is externally mixed. In SALSA, the mixing state depends on the size bin (see Table ??), and the mixing proportions are provided by the model results. In both the mass transport model and in MATCH-SALSA, the contribution to the effective refractive index of dust and black carbon is computed by the Maxwell–Garnett EMT Maxwell-Garnett (1904)(Maxwell Garnett, 1904), while for all other components we use the Bruggemann EMT (Bruggemann, 1935).

4. All other externally mixed particles not containing black carbon are assumed to be homogeneous spheres in the present version of the look-up table.

The look-up tables contain results for  $C_{\text{ext}}$ ,  $C_{\text{sca}}$ ,  $g$ , and  $C_{\text{bak}}$  in 28 wavelength bands from the UV-C to the mid-IR. Computations with the CGS model were performed for 37 discrete BC volume fractions, namely,  $f_{\text{BC}} = 0.00, 0.01, \dots, 0.20, 0.25, \dots, 1.00$ . For the shell material, as well as for non-carbon containing particles, the table contains (depending on the wavelength band) up to 40 discrete values of the real part and up to 18 discrete values of the imaginary part of the refractive index. The range of the refractive indices varies with wavelength; it is determined by those chemical components that, at each given wavelength, have the most extreme values of the refractive index. The optical properties are pre-averaged over particle sizes for each size bin. Thus we generated one

look-up table each for the mass transport model with its four size bins, and for SALSA with its 20  
390 size bins. ~~In Salsa it~~ is assumed that the number density is constant in each size bin.

The MATCH-optics model computes in each grid cell and for each size bin the effective refractive  
index of the internally mixed material by use of EMT. The corresponding optical properties are ob-  
tained by linearly interpolating the closest pre-computed results in the look-up table. Size-averaging  
is performed by weighing the optical cross sections as well as  $g \cdot C_{\text{sca}}$  in each size bin with the num-  
395 ber density per bin and adding over all bins. The integrated quantities are then divided by the total  
particle number density; the integral over  $g \cdot C_{\text{sca}}$  is also divided by the size-averaged scattering cross  
section.

## 2.4 ~~Evaluation of Methodology for comparing~~ the optics models

The new internal-mixture optics model with its BC fractal aggregate and core-grey-shell model par-  
400 ticles accounts for significant morphological details in ~~aerosols~~aerosol particles. The main question  
we want to address is whether or not this high level of detail is really necessary, i.e., if it has any  
*significant* impact on optical properties modelled with a CTM. By *significant* we mean an impact  
that is comparable to other effects whose importance is well understood. Thus to make such an  
assessment we need to pick a well-understood effect that can serve as a gauge, i.e., to which we  
405 can compare the impact of particle morphology on optical properties. We take the effect of aerosol  
~~dynamics-microphysics~~ as a gauge. As aerosol microphysics is well-known to have a substantial  
impact on aerosol concentrations and size distributions (Andersson et al., 2015; Matsui et al., 2013),  
this effect will provide us with a reference to which we can compare the impact of the morphological  
assumptions made in the aerosol-optics model. Thus we compute aerosol optical properties

- 410 1. with the MATCH mass-transport model (i.e., with aerosol ~~dynamics-microphysics~~ switched  
off), in conjunction with the old optics model (abbreviated by MT-EXT, “mass-transport ex-  
ternal mixture”);
2. with the MATCH mass-transport model in conjunction with the new optics model (MT-CGS,  
“mass-transport core-grey-shell”);
- 415 3. with the MATCH-SALSA model (i.e., with aerosol ~~dynamics-microphysics~~ switched on), in  
conjunction with the old optics model (abbreviated SALSA-EXT, "MATCH-SALSA external  
mixture");
4. with the MATCH-SALSA model, in conjunction with the new optics model (SALSA-CGS,  
“MATCH-SALSA core-grey-shell”).

420 ~~Comparison of 1. and 2. will allow~~ We first perform a comparison of monthly and geographically  
averaged differences in aerosol optical properties. More specifically, comparison of model set-ups  
MT-EXT with MT-CGS, or SALSA-EXT with SALSA-CGS allows us to assess the impact of the



morphological assumptions in the aerosol-optics model. Comparison of ~~2. and 3. MT-EXT with SALSA-EXT, or MT-CGS with SALSA-CGS~~ will give us an estimate of how much the inclusion  
425 or omission of ~~aerosol-dynamic-microphysical~~ processes impacts modelling results of aerosol radiometric properties. ~~As aerosol dynamics is well-known to have a substantial impact on aerosol concentrations and size distributions, this effect will provide us with a reference to which we can compare the impact of the morphological assumptions made in the aerosol optics model.~~

~~As an example, Fig. 4 shows the extinction aerosol optical depth (AOD) over the European model domain computed on 22 December 2007 at 12:00 with MT-EXT (left), MT-CGS (centre), and SALSA-CGS (right). The general spatial patterns are similar, as they should, since all three runs used the same EMEP emissions and HIRLAM meteorological data. However, the magnitude of the AOD results can differ significantly among the three model runs (note the semi-logarithmic scale!). Interestingly, differences~~ While statistical analyses can uncover general trends, it is difficult  
435 to understand the underlying physical reasons for model differences from an analysis of temporally and geographically averaged model results. Therefore, we also consider a few case studies in some more detail. We take the optical properties modelled with different MATCH-versions as input to a radiative transfer model and analyse the total aerosol radiative forcing and the black-carbon radiative forcing. The main goal is to understand how differences in single-scattering optical properties be-  
440 tween the two optics models (left and centre) are roughly on the same order as those between the mass-transport and aerosol dynamic models (centre and right).

~~Aerosol optical depth over Europe on 22 December 2007, 12:00 (noon). Results are shown for the mass-transport model in conjunction with the old external-mixture optics model (left), and with the new internal-mixture/core-grey-shell/fractal BC aggregate model (center), as well as for the~~ MATCH-SALSA model in conjunction with the new optics model (right). The circles indicate the four locations used for radiative transfer studies. Note the semi-logarithmic colour scale!  
445

~~Thus a first inspection of computed fields of aerosol optical properties suggests that the level of detail in the morphological assumptions of the aerosol optics model may be significant for the modelling results. In a next step we quantify differences in modelled aerosol radiative forcing~~ among the three model versions. To this end we pick impact the outcome of the radiative transfer simulations. To keep the case studies within manageable bounds, we restrict ourselves to four geographic locations that are indicated by circles in Fig. 4; (two over land, two over the ocean), two instances (one representing low-BC summer concentrations, one representing high-BC winter conditions), and we limit ourselves to comparing the model set-ups MT-EXT, MT-CGS, and SALSA-CGS.  
455 More specifically, we consider one site over Northern Italy (45.0° N, 8.5° E), one over the Mediterranean Sea (37.5° N, 5.5° E), one over Poland (52.6° N, 21.0° E), and one over the North Sea (52.0° N, 2.7° E). ~~We further pick two instances representing low-BC summer and high-BC winter conditions, namely,~~ For the two instances, we pick 22 June 2007 12:00 UTC, and 22 December 2007 12:00 UTC. Radiative transfer calculations are performed for each of these four sites and for

460 both instances. Vertical profiles of the aerosol optical depth per layer, the single-scattering albedo, and the asymmetry parameter are used as input to the libRadtran radiative transfer package (Kylling et al., 1998), assuming a plane-parallel atmosphere. For the surface albedo of the ocean we assume a spectrally constant value of 0.065, while for the spectrally varying surface albedo of the two land locations we used MODIS observations for each of the two instances. The results were spectrally  
465 integrated to obtain the broadband radiative fluxes. The radiative transfer simulations were repeated for corresponding profiles of optical properties (with a 1 km resolution) in the absence of black carbon, as well as for clear-sky conditions. This allows us to compute differences in broadband radiative fluxes, i.e., the radiative effect of black carbon, and the radiative effect of all ~~aerosols~~aerosol components. The results of this radiative transfer study are discussed in Sect. 3.2.

470 To further investigate the significance of the optics model on radiometric properties, we ~~look at remote sensing related optical properties~~ also look at optical properties relevant for remote sensing, namely, backscattering coefficient and Ångström exponent. These results are discussed in Sects. 3.3 and 3.4, respectively.

### 3 Results

#### 475 3.1 Aerosol optical properties in MATCH

Figure 4 gives us a first impression of the differences among the four model configurations. The extinction AOD is shown for MT-EXT (1st from the left), MT-GCS (2nd), Salsa-CGS (3rd) and Salsa-EXT (4th). The overall spatial patterns are similar. This is expected, since all model configurations used the same EMEP emissions and HIRLAM meteorological data. However, the magnitude of the  
480 AOD results can differ significantly among the four model runs (note the semi-logarithmic scale!). It is also remarkable that the differences between the two optics models depend on whether we make this comparison within the mass-transport model (compare MT-EXT to MT-CGS), or within Salsa (compare SALSA-CGS and Salsa-EXT). It can also vary geographically. This merely confirms the complexity of aerosol-optics modelling. Replacing one optics model by another will not simply  
485 offset the resulting optical properties by some common factor; it will introduce a significant change in modelled optical properties, of which the magnitude and even the sign can be dependent on local conditions, such as the size-distribution and the chemical composition of the aerosol particles.

This is also evident from a comparative analysis of geographically and temporally averaged aerosol optical properties. Table 4 shows aerosol optical depth (AOD), backscattering coefficient  
490 (BSCA), single scattering albedo (SSA) and asymmetry parameter (g), each at three different wavelengths (355, 532, and 1064 nm), and each averaged over the whole model domain and over one month (December 2007). The columns show relative differences; for instance,  $MT(EXT,CGS)=(MT-EXT - MT-CGS)/(MT-CGS)$  is the relative difference of MT-model results obtained with the EXT and CGS optics models.

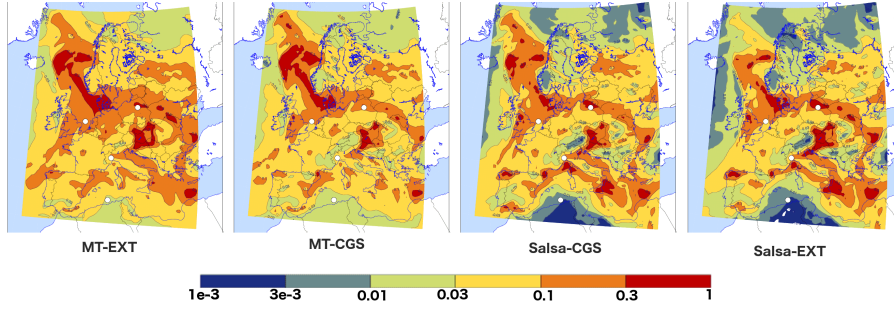


**Figure 4.** Aerosol optical depth over Europe on 22 December 2007, 12:00 UTC (noon). Results are shown for the mass transport model in conjunction with the old external-mixture optics model (1st to the left), and with the new internal-mixture/core-grey-shell/fractal BC aggregate model (2nd to the left), as well as for the MATCH-SALSA model in conjunction with the new optics model (3rd to the left) and old optics model (4th to the left). The circles indicate the four locations used for radiative transfer studies. Note the semi-logarithmic colour scale!

**Table 4.** Averaged relative difference in aerosol optical depth (AOD), backscattering coefficient (BSCA), single scattering albedo (SSA) and asymmetry parameter (g), among the different model set-ups for December 2007. The average has been performed over a whole month and over all grid-cells (horizontally for AOD, horizontally and vertically for all other optical properties). Each number corresponds to a relative difference between two model set-ups. For instance,  $MT(EXT,CGS) = (MT-EXT - MT-CGS)/(MT-CGS)$  compares results obtained with the mass transport model (MT) by using the two different optics models (EXT and CGS).

$X_{\lambda, [nm]}$	MT(EXT,CGS)	Salsa(EXT,CGS)	CGS(MT,Salsa)	EXT(MT,Salsa)
$AOD_{355}$	0.16	-0.28	-0.50	-0.19
$AOD_{532}$	0.08	-0.14	0.00	0.25
$AOD_{1064}$	0.18	-0.03	0.14	0.37
$BSCA_{355}$	0.44	-0.01	-0.47	-0.23
$BSCA_{532}$	0.26	-0.08	-0.19	0.11
$BSCA_{1064}$	0.99	-0.01	-0.36	0.28
$SSA_{355}$	-0.02	0.04	0.03	-0.03
$SSA_{532}$	-0.02	0.05	0.04	-0.02
$SSA_{1064}$	-0.07	0.08	0.08	-0.07
$g_{355}$	0.06	-0.01	-0.10	-0.03
$g_{532}$	0.10	-0.00	-0.06	0.04
$g_{1064}$	0.17	-0.02	-0.11	0.06

495 Comparison of the columns "MT(EXT,CGS)" and "Salsa(EXT,CGS)" illustrates the differences  
between the optics models in the absence and presence of aerosol-microphysical processes. As  
we already suspected from inspection of Fig. 4, differences in the optics models defy simplistic  
explanations; both the magnitude and sign of these difference can be strongly dependent on the  
size-dependent chemical composition and mixing state of the aerosols, hence on the model version  
500 with which the optics models are being compared. In our case, we see that compared to the CGS  
model, the EXT-optics model predicts higher values of AOD, BSCA, and  $g$  in the MT model, and  
lower values of SSA. In Salsa the roles of the CGS and EXT model are reversed.

The column "CGS(MT,Salsa)" shows differences between optical properties computed in the  
absence and presence of aerosol-microphysical processes, where the optics-computations have been  
505 performed with the CGS model. The column "EXT(MT,Salsa)" shows an analogous comparison,  
where the optics-computations have been performed with the EXT model. If we compare the magnitudes  
of the entries in the columns "MT(EXT,CGS)" and "Salsa(EXT,CGS)" with the corresponding magnitudes  
of the entries in the columns "CGS(MT,Salsa)" and "EXT(MT,Salsa)", then we see that the differences  
between the two optics models (EXT,CGS) are roughly on the same order as the differences between  
510 the two aerosol models (MT,Salsa). Thus, the main observation is that the choice of aerosol-optics  
model can have an effect on modelled optical properties that is of comparable magnitude as the level  
of detail in the description of aerosol-microphysical processes.

While spatio-temporally averaged model results allows us to draw some general conclusions, it  
is difficult to understand the reasons for the observed differences from such an analysis. We will,  
515 therefore, complement this investigation in the following sections with a more detailed analysis of  
some selected case studies.

### 3.2 Optical properties and radiative forcing

In Sec. 2.3.2 we have discussed how morphological properties of aerosol particles can impact their  
optical properties. We now take this one step further and discuss how the optical properties of  
520 particles can impact the radiative properties of an aerosol-laden atmosphere. We will show results  
for a single wavelength near the maximum of the solar spectrum. The comparison will focus on  
three model set-ups, MT-EXT, MT-CGS, and Salsa-CGS. We will use MT-CGS as a reference and  
compare it first to Salsa-CGS in order to investigate the impact of aerosol-microphysics (MT versus  
Salsa). Next, we compare MT-CGS to MT-EXT in order to investigate the impact of the optics model  
525 (CGS versus EXT).

The result for the optical properties obtained with the three model versions (AOD per layer,  
SSA and  $g$ ) at the wavelength 532(CGS)/500(EXT) nm, together with the radiative forcing for  
aerosols all aerosol component and black carbon, respectively, can be seen in Figs. 5–10 for North-  
ern Italy and the Mediterranean on 22 June 2007. Each figure shows the differences in direct solar  
530 flux  $\Delta F_s$  (top left), diffuse downwelling flux  $\Delta F_d$  (top right), diffuse upwelling flux  $\Delta F_u$  (centre

left), and net radiative flux  $\Delta F_{\text{net}} = \Delta F_s + \Delta F_d - \Delta F_u$  (centre right), where either the difference between aerosol-laden and clear sky conditions are considered (Figs. 5 and 6), or the difference between fluxes in the presence and absence of black carbon (Figs. 9 and 10). ~~Top-of-atmosphere~~ Here, downwelling fluxes are obtained by integrating the radiance over all azimuthal angles, and over polar angles from 90° to 180°, where the positive z-axis is directed from the ground to the top-of-atmosphere (TOA). Similarly, the upwelling flux is obtained by integrating the radiance over all azimuthal angles, and over polar angles from 0 to 90°. TOA results for the other geographical locations are summarized in Table 5 in terms of aerosol forcing ~~in Table 5 and black carbon forcing~~ ( $\Delta F_{\text{net}} = F_{\text{net}}(\text{with aerosol particles}) - F_{\text{net}}(\text{no aerosol particles})$ ), and in Table 6 in terms of black-carbon forcing ( $\Delta F_{\text{net}} = F_{\text{net}}(\text{with black carbon}) - F_{\text{net}}(\text{no black carbon})$ ). The wavelengths 532(CGS)/500(EXT) nm are near the maximum of the solar spectrum. ~~At other wavelengths (not shown) the optical properties behave similarly.~~ Each figure has a vertical span of 65 km, which comprises that part of the troposphere where ~~almost all aerosols~~ most aerosol particles are concentrated in the cases we picked.

~~Before starting our analysis, we note that the magnitude of the radiative fluxes generally depends on the concentration of aerosols. As we cannot claim that the test cases we happened to pick are in any way representative for typical aerosol and black carbon loads, we are not focusing on the magnitude of the radiative fluxes here. Rather, we want to compare the differences in radiative fluxes among the three model versions.~~

### 550 3.2.1 Comparison of ~~aerosol dynamics~~ aerosol microphysics and mass-transport model

We start by comparing radiative fluxes in the presence and absence of ~~aerosols~~ all aerosol components, which we refer to as the “aerosol radiative effects”. Figures 5 and 6 show the aerosol radiative effects modelled over Northern Italy and over the Mediterranean north of ~~Algier~~ Algiers, respectively. The general patterns in both plots can be understood as follows. In the presence of ~~aerosols~~ all aerosol components, optical extinction is stronger than in clean air. Thus the presence of ~~aerosols~~ all aerosol components gives a reduction  $\Delta F_s$  of the direct solar flux (upper left). As the aerosol optical depth per atmospheric layer strongly increases near the ground, the magnitude of  $\Delta F_s$  increases sharply with decreasing altitude. Further, ~~aerosol extinction~~ extinction in the form of scattering results in the generation of diffuse flux; the downwelling diffuse flux accumulates downward, resulting in an increasing excess of downwelling flux  $\Delta F_d$  in the presence of ~~aerosols~~ aerosol components as one approaches the surface. The upwelling flux  $F_u$  is generated by scattering in the atmosphere and reflection at the surface. Since aerosol extinction reduces the ~~total-net radiative~~ flux as one approaches the surface, less upwelling diffuse flux is generated at low altitudes; hence the difference in upwelling flux  $\Delta F_u$  between an aerosol-laden and a clear sky atmosphere is negative near the surface. However, it increases with altitude, because at higher altitudes the magnitude of the difference (aerosol –

clear sky) in the ~~total net radiative~~ flux that can be converted into upwelling diffuse flux decreases at higher altitudes.

If we focus now on differences in the radiative net flux  $\Delta F_{\text{net}}$  at high altitudes, i.e., the radiative forcing effect of ~~aerosols~~ aerosol particles, then we see significant differences between the mass transport model (MT, red) and SALSA (green) at both geographic locations. It is evident that the  
 570 main cause for these are corresponding differences in the diffuse upwelling flux  $\Delta F_{\text{u}}$ .

At both locations the diffuse upwelling flux is smaller for SALSA than for MT, but for different reasons. Over the Mediterranean (Fig. 6), the AOD is significantly smaller for SALSA than for MT, resulting in less extinction of the direct flux, hence less generation of diffuse flux, and a smaller  
 575 radiative cooling effect for SALSA.

Over Northern Italy (Fig. 5), there is almost no difference in AOD between the two models. It can be seen from the AOD profile that the majority of ~~aerosols~~ aerosol particles reside in the lowest 1 km near the surface. However, above 1 km the results of  $\Delta F_{\text{u}}$  obtained with SALSA and MT diverge with increasing altitude. This is a result of the reflection by the near-surface aerosol layer, which  
 580 is ~~slightly~~ different in the two models. In MT the SSA is higher than in SALSA, resulting in more scattering, thus in more diffuse radiation. The asymmetry parameter is ~~slightly~~ larger in MT than in SALSA; correspondingly, the partitioning in MT between downwelling and upwelling radiation is somewhat shifted in favour of the former. However, this only partially counteracts the generation of a higher amount of diffuse upwelling radiation in MT due to the higher SSA. The net effect is  
 585 a higher value of  $\Delta F_{\text{u}}$  in MT, hence a larger radiative cooling effect at higher altitudes.

To further analyse the difference in optical properties between MT and SALSA, we look at the aerosol masses and the relative sizes of the particles. Figure 7 shows vertical profiles of the effective radius ~~of the size distributions~~  $r_{\text{eff}}$  defined according to Eq. 1, in SALSA (green) and the MT model (black) over Northern Italy (left) and over the Mediterranean (right).

$$590 \quad r_{\text{eff}} = \frac{\int_0^{\infty} n(r) \pi r^2 \cdot r dr}{\int_0^{\infty} n(r) \cdot \pi r^2 dr} \quad (1)$$

Figure 8 shows profiles for the total aerosol mass (1st row), BC (black carbon) (2nd row), sulphate (3rd row), and nitrate (4th row) for both Northern Italy (1st column) and Mediterranean (2nd column). We focus on the total aerosol mass, which is expected to impact the aerosol optical depth. The aerosol optical depth is dependent on the number density (which, in turn, increases with the mass  
 595 mixing ratio), as well as on the extinction cross section (which generally increases with the effective radius of the particles). Over Northern Italy, the SALSA model predicts a larger mass mixing ratio than the MT model (Fig. 8, upper left) ~~,but also and~~ a smaller particle size (Fig. 7, left). This results in a higher number density but a smaller extinction cross section. These two effects cancel almost exactly, resulting in nearly identical aerosol optical depths predicted with the two models (Fig. 5,  
 600 bottom left). By contrast, over the Mediterranean the two models predict similar mass mixing ratios (Fig. 8, upper right), while SALSA predicts a much lower effective radius than the MT model

(Fig. 7, right). As a consequence, the optical depth is significantly lower in SALSA than in MT (Fig. 6, bottom left). The SSA is lower in SALSA than in MT. This is mainly caused by the fact that the effective radius is smaller in SALSA than in MT, since SSA is usually increasing with size.

605 ~~The radiative impacts~~ For the other two geographical locations and the second time event, the TOA results are summarised in Table 5 ~~show the same behaviour as Figs. 5 and 6 at three of the four geographical locations. The Polish site deviates, since SALSA produces a much larger radiative cooling than the MT model.~~ Over the North Sea, Northern Italy, and the Mediterranean the TOA forcing is strongest in the MT-EXT model (mass transport with old optics model), it is smaller  
610 in the MT-CGS model (mass transport with new optics model), and weakest in the SALSA-CGS model (aerosol-microphysics with new optics model). However, over Poland the negative forcing in SALSA-CGS is strongest among the three models in the summer, and second strongest in the winter. This can be explained by SALSA having a larger amount of ~~aerosols~~ aerosol particles throughout the column at that site, especially more sulphate, which, when externally mixed, contributes to a larger  
615 amount of scattering and therefore a higher SSA and a larger diffuse upwelling radiative flux.

We now compare radiative fluxes in the presence and absence of black carbon, which we refer to as the “black carbon radiative effect”. Figures 9 and 10 show the radiative effect of black carbon together with the optical properties with and without black carbon. Again, ~~the dominant feature of differences in~~  $\Delta F_{\text{net}}$  at TOA ~~comes from~~ are mainly caused by corresponding differences in the  
620 upwelling diffuse radiative flux  $\Delta F_{\text{u}}$ . In these figures, we have to focus on the difference in the optical properties when analysing the radiative fluxes. The general pattern can be seen in Fig. 9, which shows the differences in radiative fluxes and in the optical properties over Northern Italy. The direct solar flux (upper left) decreases with decreasing altitude owing to extinction. The magnitude of the decrease mainly reflects the differences in optical depth in the presence and absence of black carbon  
625 (bottom left), which is ~~slightly~~ larger in SALSA than in MT. The decrease in solar flux does not automatically result in an increase in the downwelling diffuse flux with decreasing altitude (upper right), as it was in the comparison of fluxes in the presence and absence of ~~all aerosols~~ aerosol components. The situation is more complex now. Near the surface, where the optical depth is largest, the difference in SSA in the presence and absence of black carbon is ~~quite~~ large in the MT model (bottom  
630 centre, red lines), and ~~slightly~~ smaller in SALSA (green lines). As a result, absorption contributes more to the total extinction in the MT model than in SALSA (at least near the surface). Hence, the portion of the downwelling flux that is absorbed on its way downward is larger in the MT model than in SALSA, resulting in a decrease of the diffuse downwelling flux with decreasing altitude (upper  
635 right, red line). The differences between the two models in the diffuse upwelling flux are very small (centre left, red and green lines). This is the result of cancelling effects; for instance, there is less direct solar flux, but more diffuse downwelling flux in SALSA that can be converted into diffuse upwelling flux through scattering. As a result, the differences between both models in the net flux (centre right, red and green lines) are almost negligible.

Figure 10 shows the radiative effect of black carbon over the Mediterranean. Again, ~~the dominant~~  
640 ~~feature of differences in  $\Delta F_{\text{net}}$  at TOA comes from are mainly caused by~~ corresponding differ-  
ences in the upwelling diffuse radiative flux  $\Delta F_{\text{u}}$ . ~~The difference between MT and SALSA are not~~  
~~as prominent here, mainly due to the fact that the differences in the optical properties are similar,~~  
~~especially in the SSA. There is still a small difference for the Mediterranean, where SALSA has~~  
~~a larger radiative cooling than MT. This difference is very small, but it may come from the slight~~  
645 ~~difference in the AOD combined with the difference in SSA from above 1, where SALSA has~~  
~~a marginally larger difference than MT, creating the difference in the net radiative flux above 1.~~  
~~Another possibility is that these small differences are caused by multiple scattering effects, which~~  
~~are notoriously difficult to understand by an intuitive approach. If studying the differences in AOD~~  
~~and SSA for the twelve wavelengths used in this study (not shown), the differences for SALSA~~  
650 ~~AOD and SSA are smaller for the long-wave (LW) part of~~ only differ by a few  $\text{mW}/\text{m}^2$ . The main  
reason is that the optical properties, especially the spectrum (533.2–3461.5). ~~This results in less LW~~  
~~extinction and scattering and slightly more radiative cooling for SALSA.~~ SSA, differ in the presence  
and absence of BC by almost the same amount in both models.

Table 6 shows the black carbon forcing for all the four geographical locations and both months.  
655 ~~In June the difference at the TOA is very small between MT and SALSA for all the locations,~~  
~~but larger for the Mediterranean as noted in Fig. 10. The month of December shows a pattern~~  
~~where SALSA has a higher radiative heating over land, and smaller over the ocean compared~~  
~~to MT. This is strongly coupled to the larger difference in BC amounts over land than over the~~  
~~oceans, where the two models have similar values all through the column, see Fig. 8.~~ As a general trend,  
660 large differences in BC concentrations are visible as corresponding differences in BC forcing. For  
instance, near-surface BC winter- concentrations in Northern Italy are about a factor of 10 higher  
than in summer; summer-concentrations over the Mediterranean are more than a factor of 2 higher  
than in winter; in Northern Italy in winter, Salsa predicts more than 2 times higher BC-concentrations  
than the mass-transport model, while over the Mediterranean in winter the role of the two models  
665 is reversed (not shown). All of this corresponds with the respective BC-forcing rates in Table 6.  
However, when the differences in BC-concentrations are small, then there is no clear relation between  
the concentration-differences and the corresponding differences in BC-forcing rates. For instance,  
as we see in Fig. 8, there is almost no difference between the BC-concentrations computed with  
the two models over the Mediterranean in summer. But the table shows that the mass-transport  
670 model predicts a slightly higher forcing rate than SALSA. A possible cause is the difference in the  
size-distributions in SALSA and the mass-transport model. ~~For Northern Italy and Mediterranean-~~  
~~Poland and North Sea are not shown here, but show similar behaviour.~~



### 3.2.2 Comparison of the two optics models

The comparison between SALSA and the MT model in the previous section served two purposes.

675 First, it helped us to develop a basic understanding for the effects of ~~aerosols~~ aerosol particles and black carbon on radiative fluxes. Second, it provided us with a gauge for assessing the importance of the ~~aerosol-optics~~ aerosol-optics model, which will be the subject of this section.

~~Aerosol forcing and optical properties at 532(CGS)/500(EXT) nm for Northern Italy in June.~~

~~Aerosol forcing and optical properties at 532(CGS)/500(EXT) nm for the Mediterranean in June.~~

680 ~~The aerosol forcing at the top of the atmosphere (TOA),  $\Delta F_{\text{net,TOA}} - W$ , for the four different geographical locations, one summer and one winter event, and three model versions: MT-EXT MT-CGS SALSA-CGS SummerPoland -0.21 -0.21 -0.77 North Sea -0.34 -0.29 -0.24 Northern Italy -0.06 -0.05 0.01 Mediterranean -1.20 -0.99 -0.30 WinterPolen -4.41 -2.00 -2.18 North Sea -2.85 -1.21 -0.86 Northern Italy -1.15 -0.53 -0.57 Mediterranean -0.09 -0.04 -0.03~~

685 We compare the old EXT (blue line) and the new CGS (red line) optics models in Figs. 5 and 6, each used in conjunction with the MT-version of MATCH. The net radiative flux  $\Delta F_{\text{net}}$  in the CGS model shows a weaker TOA cooling effect than the EXT model, both over Northern Italy and over the Mediterranean. Again, the upwelling flux has the dominant impact on the behaviour of the TOA net radiative flux. Over Northern Italy (Fig. 5) the diffuse upwelling flux is larger for the EXT model  
690 above 1 km, whereas it is smaller below 1 km and at the bottom of the atmosphere (BOA). The AOD profile reveals that in the EXT model extinction is stronger than in the CGS model throughout the tropospheric column. As a result, there is more diffuse downwelling flux being generated in EXT than in CGS. At the bottom of the atmosphere (BOA) extinction of the direct flux is stronger than generation of diffuse downwelling flux; hence less downwelling flux is reflected by the surface,  
695 resulting in less BOA upwelling diffuse flux in EXT than in CGS. Higher up in the troposphere, the upwelling diffuse flux is mostly generated by atmospheric scattering rather than reflection from the surface. As the SSA in EXT is higher than in CGS, more diffuse flux is generated, resulting in a stronger radiative cooling effect in EXT than in CGS.

Over the Mediterranean (Fig. 6), the EXT and CGS model have almost identical AOD profiles in  
700 the green part of the spectrum. However, at longer wavelengths (~~not shown~~) EXT predicts substantially higher AOD values than CGS (see (see Appendix E, Fig. 16). For instance, at  $\lambda = 1020$  nm the near-surface AOD per layer computed with the EXT-model is about twice as high as that computed with the CGS-model.) This explains the larger amount of diffuse broadband radiation generated in the EXT model, which results in a stronger negative TOA net flux in EXT as compared to the CGS  
705 model. Note that the differences in SSA between EXT and CGS are ~~fairly small~~ less than 0.03, while the differences in  $g$  are ~~rather large~~ as much as 0.07. The higher values of  $g$  in EXT may contribute to the large amount of diffuse ~~downwelling~~ downwelling radiation in that model; however, the dominant effect is likely to be the high optical depth at red and IR wavelengths (see Appendix E).

**Table 5.** The aerosol forcing at the top of the atmosphere (TOA),  $\Delta F_{\text{net,TOA}}$  [ $\text{W m}^{-2}$ ], for the four different geographical locations, one summer (2007-06-22, 12:00) and one winter (2007-12-22, 12:00) event, and three model versions, MT-EXT, MT-CGS and Salsa-CGS.

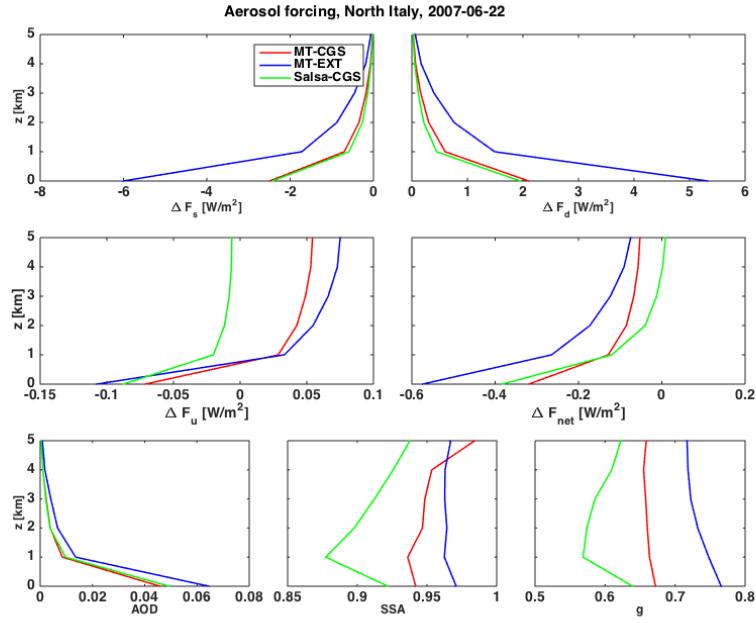
		<u>MT-EXT</u>	<u>MT-CGS</u>	<u>SALSA-CGS</u>
<u>Summer</u>	<u>Poland</u>	<u>-0.21</u>	<u>-0.21</u>	<u>-0.77</u>
	<u>North Sea</u>	<u>-0.34</u>	<u>-0.29</u>	<u>-0.24</u>
	<u>Northern Italy</u>	<u>-0.06</u>	<u>-0.05</u>	<u>0.01</u>
	<u>Mediterranean</u>	<u>-1.20</u>	<u>-0.99</u>	<u>-0.30</u>
<u>Winter</u>	<u>Poland</u>	<u>-4.41</u>	<u>-2.00</u>	<u>-2.18</u>
	<u>North Sea</u>	<u>-2.85</u>	<u>-1.21</u>	<u>-0.86</u>
	<u>Northern Italy</u>	<u>-1.15</u>	<u>-0.53</u>	<u>-0.57</u>
	<u>Mediterranean</u>	<u>-0.09</u>	<u>-0.04</u>	<u>-0.03</u>

Table 5 summarises the TOA net radiative flux at all four geographical locations for both June and  
 710 December. The largest differences among the models are seen in December at the two northernmost  
 locations, i.e., Poland and the North Sea. At these two places, the total aerosol amount (not shown)  
 is significantly higher than at the other two locations farther south, giving rise to a larger absolute  
 changes in the aerosol forcing.

The black carbon forcing ~~looks rather different at the two geographical locations~~ in Fig. 9 (Northern  
 715 Italy) and 10 (Mediterranean) display different behaviours in radiative fluxes, comparing the EXT  
 (blue) and CGS (red) model results. Over Northern Italy, the net black carbon forcing is more sig-  
 nificant than over the Mediterranean in Fig. 10 due to higher levels of BC, see Fig. 8. As can be seen  
 in Fig. 9, the differences in optical properties computed with and without black carbon are larger in  
 the CGS model than in the EXT model, particularly for the SSA. This means that in the CGS model  
 720 the presence of black carbon causes more absorption than in the EXT model, thus generating less  
 diffuse down- and upwelling flux by scattering. As a result, the CGS model predicts more radiative  
 warming, i.e., a higher TOA radiative net flux than the EXT model. The reason for this is that (i)  
 the CGS model treats externally mixed soot as aggregates, which have a lower SSA than the mas-  
 sive black carbon spheres in the EXT model; and (ii) the CGS model treats internally mixed soot as  
 725 a coated core-grey-shell model, which accounts for focusing of electromagnetic radiation onto the  
 carbon core, thus enhancing absorption, i.e., lowering the SSA, while the EXT model treats all black  
 carbon as externally mixed.

~~Effective radius for the two chemical transport model versions MT and SALSA over Northern  
 Italy and Mediterranean in June.~~

730 ~~Vertical distribution of aerosols at Northern Italy and Mediterranean in June.~~



**Figure 5.** Aerosol forcing and optical properties at 532(CGS)/500(EXT) nm over Northern Italy in June. Results are shown for the three model versions MT-EXT (blue), MT-CGS (red) and Salsa-CGS (green). The aerosol forcing is derived by taking the difference in radiative fluxes between an aerosol laden and a clear sky. The difference in direct ( $\Delta F_s$ ) and diffuse ( $\Delta F_d$ ) downwelling, as well as the diffuse upwelling ( $\Delta F_u$ ) and the net radiative flux (aerosol forcing) ( $\Delta F_{\text{net}} = \Delta F_s + \Delta F_d - \Delta F_u$ ) are shown in the first four figures (1st and 2nd row of plots). The optical properties aerosol optical depth (AOD), single scattering albedo (SSA) and asymmetry parameter ( $g$ ) are shown in the 3rd row of plots.

**Table 6.** The Same as table 5, but for black carbon forcing at the top of the atmosphere (TOA),  $\Delta F_{\text{net,TOA}}$  W, for the four different geographical locations, one summer and one winter event, and three model versions.

		MT-EXT	MT-CGS	SALSA-CGS
Summer	Poland	$1.02 \times 10^{-2}$	$1.16 \times 10^{-2}$	$1.20 \times 10^{-2}$
	North Sea	$1.71 \times 10^{-2}$	$1.54 \times 10^{-2}$	$1.49 \times 10^{-2}$
	Northern Italy	$4.61 \times 10^{-2}$	$7.77 \times 10^{-2}$	$7.86 \times 10^{-2}$
	Mediterranean	$8.54 \times 10^{-3}$	$6.45 \times 10^{-3}$	$2.41 \times 10^{-3}$
Winter	Poland	$4.03 \times 10^{-2}$	$3.56 \times 10^{-2}$	$6.83 \times 10^{-2}$
	North Sea	$1.95 \times 10^{-2}$	$2.28 \times 10^{-2}$	$4.97 \times 10^{-3}$
	Northern Italy	$6.73 \times 10^{-2}$	$1.08 \times 10^{-1}$	$1.46 \times 10^{-1}$
	Mediterranean	$6.03 \times 10^{-4}$	$1.34 \times 10^{-3}$	$3.13 \times 10^{-4}$

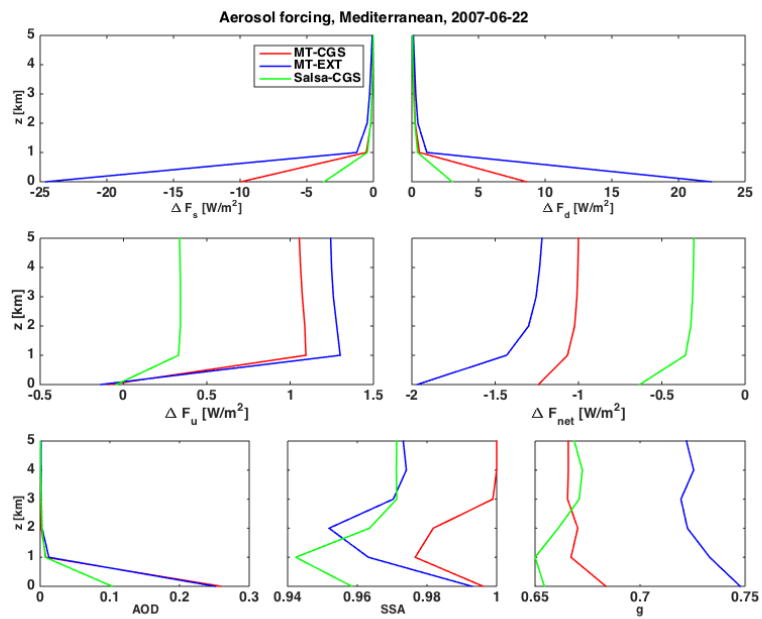


Figure 6. Same as figure 5 but over the Mediterranean.

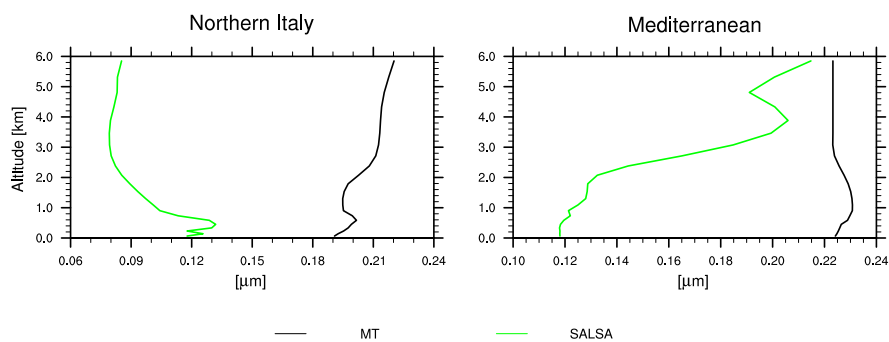
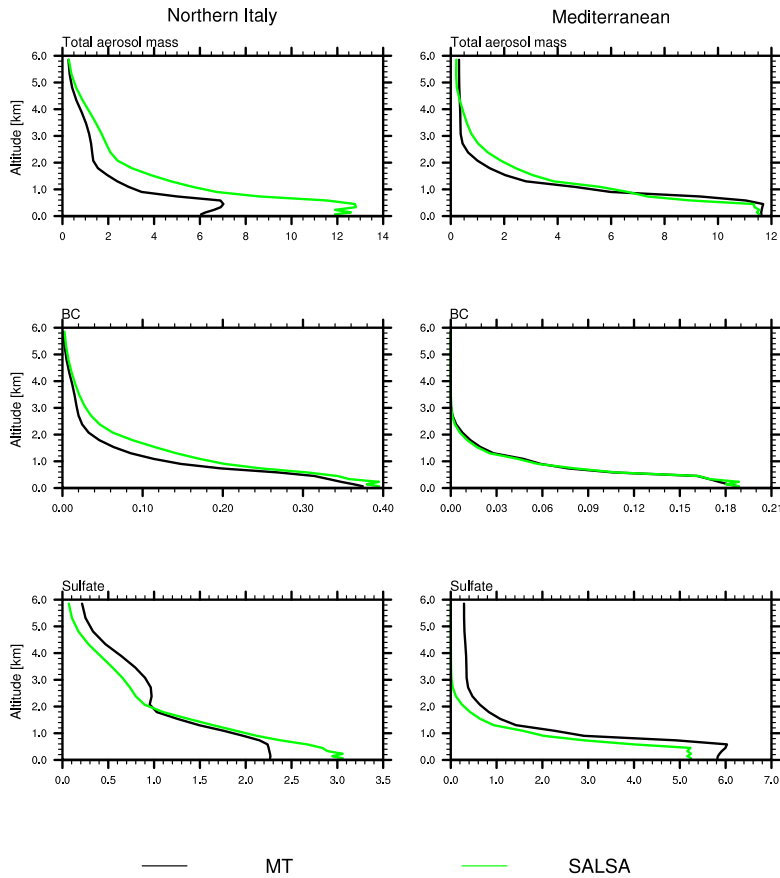


Figure 7. Black carbon forcing and optical properties at 532(CGS)/500(EXT) nm Effective radius,  $r_{eff}$ , for the two chemical transport model versions MT and SALSA over Northern Italy in June and Mediterranean the 2007-06-22 at 12:00.



**Figure 8.** Vertical distribution of aerosol particles in Northern Italy and over the Mediterranean on 2007-06-22 at 12:00.

### 3.3 Gauging the significance of aerosol optics modelling

Now that we have understood the impact of the aerosol optical properties on radiative fluxes, we finally turn Let us now return to the main question of this study. We ask if, namely, whether or not the level of detail in aerosol optics modelling has a significant impact on observable radiometric properties. As a gauge we consider the changes in radiometric properties We already saw in Table 4 that, on average, the effect of including aerosol microphysics on optical properties is of comparable magnitude as the effect caused by the inclusion or omission of aerosol dynamic processes. Thus we morphological assumptions in the aerosol optics model. However, we also saw that the magnitude and sign of these impacts can be quite variable and depending on several factors. We find this confirmed in the analysis of our radiative-transfer study. More specifically, we can compare in Figs. 5–10 the differences in radiative forcing between the MT-CGS and Salsa-CGS (red and green lines) to the corresponding differences in the between MT-CGS and MT-EXT (red and blue

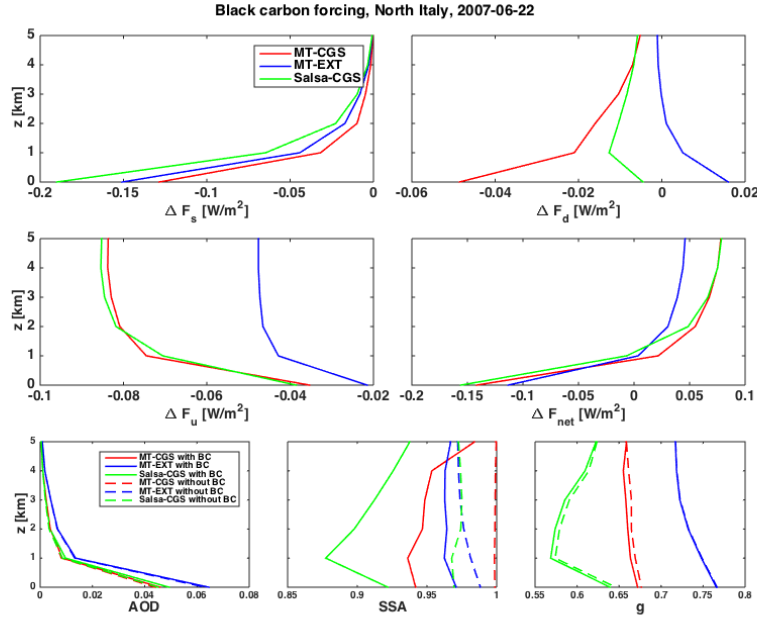


**Figure 9.** Black carbon forcing and optical properties at 532(CGS)/500(EXT) nm over Northern Italy in June. Results are shown for the three model versions MT-EXT (blue), MT-CGS (red) and Salsa-CGS (green). The black carbon forcing is derived by taking the difference in radiative fluxes between an aerosol laden including black carbon and an aerosol laden sky omitting black carbon. The difference in direct ( $\Delta F_s$ ) and diffuse ( $\Delta F_d$ ) downwelling, as well as the diffuse upwelling ( $\Delta F_u$ ) and the net radiative flux (aerosol forcing) ( $\Delta F_{net} = \Delta F_s + \Delta F_d - \Delta F_u$ ) are shown in the first four figures (1st and 2nd row of plots). The optical properties aerosol optical depth (AOD), single scattering albedo (SSA) and asymmetry parameter (g) are shown in the 3rd row of plots.

lines). We see that in some cases the choice of optics model has a stronger effect than the inclusion of aerosol dynamics-microphysics (e.g. Fig. 9), while in other cases it is the other way round (e.g. 745 Fig. 6). We can also inspect Tables 5 and 6 and arrive at the same result. **On average, the effect of including aerosol dynamics on the TOA radiative forcing is of comparable magnitude as the effect caused by employing a more realistic aerosol optics model.**

In the following two subsections, we will focus on the selected case-studies and discuss the significance of the optics model for radiometric quantities that are relevant for remote sensing applications.

### 750 3.3 Backscattering coefficient

From ground-based and space-borne lidars-lidar measurements one can obtain the aerosol backscattering coefficient  $\beta$ , which is proportional to the backscattering cross section  $C'_{bak}$  of the particles and the aerosol number density. Figure 11 shows vertical profiles of  $\beta$  computed at two locations

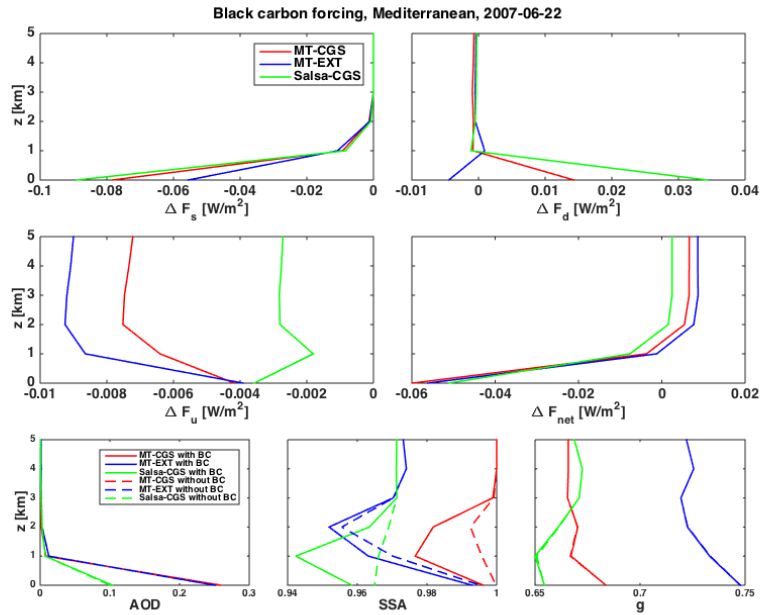


**Figure 10.** Black carbon forcing and optical properties at 532(CGS)/500(EXT) nm for ~~Same as Figure 9, but~~ over the Mediterranean in June.

and at two instances, as indicated in the figure headings. Each panel shows computational results  
 755 obtained with the three different model versions. The figure shows results for the second Nd:YAG  
 harmonic of 532 nm. Corresponding results computed for wavelengths of 355 and 1064 nm lead to  
 similar conclusions.

We saw in Fig. 8 for June over Northern Italy (upper left) that SALSA predicts an aerosol mass  
 mixing ratio, hence a particle number density, that is higher than that in the MT model. But we also  
 760 saw in Fig. 7 (left) that SALSA predicts lower values of  $r_{\text{eff}}$ . This results in lower values of  $C_{\text{bak}}$ . We  
 see in Fig. 11 (upper left) that the effect on  $\beta$  of the higher number density dominates over the effect  
 of the lower  $r_{\text{eff}}$ , resulting in values of  $\beta$  that are about 30 % higher in SALSA (green line) than in the  
 MT model (red line). Over the Mediterranean, both SALSA and the MT model predict similar mass  
~~densities mixing ratios~~ (Fig. 8, upper right); but SALSA still predicts substantially lower values of  
 765  $r_{\text{eff}}$  (Fig. 7, right). The result is that  $\beta$  computed with the MT model (red line) is almost twice as  
 high as the corresponding results obtained with SALSA (green line) (Fig. 11, upper right).

A similar comparison of the two optics models (red and blue lines in Fig. 11) shows that the  
 new CGS optics model consistently predicts substantially lower values of  $\beta$  than the old EXT optics  
 model. This agrees with the comparison shown in Kahnert et al. (2013) between encapsulated black  
 770 carbon aggregates and externally mixed homogeneous spheres. (In a retrieval algorithm, an optics  
 model that overestimates the backscattering cross section would result in underestimated retrieval

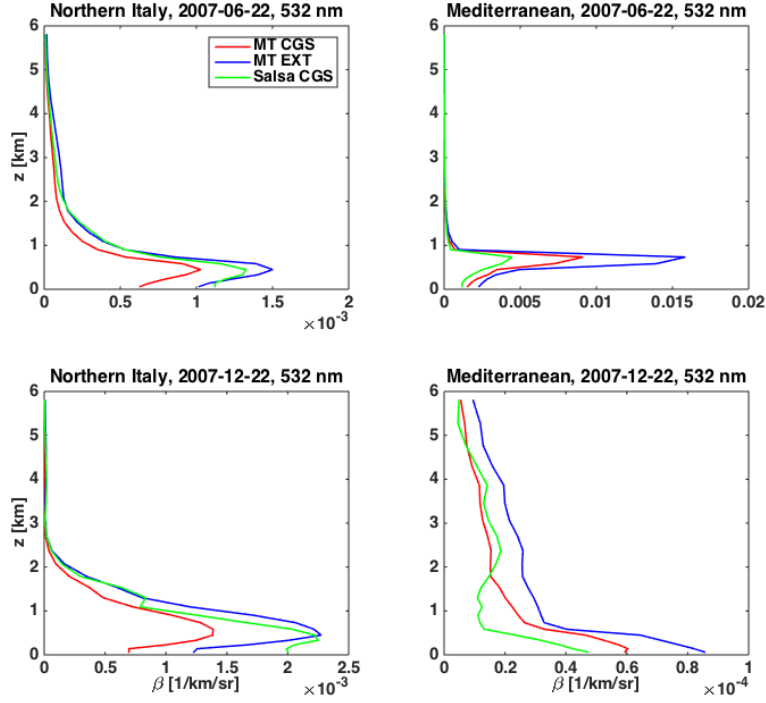


**Figure 11.** Backscattering coefficient at a wavelength of 532 nm at two different locations Northern Italy and Mediterranean and at two different instances time events (22/6 and 22/12-2007 at 12.00), computed with the three model versions, MT-EXT (blue), MT-CGS (red) and Salsa-CGS (green).

results for the particle number density.) The differences between the two optics models are on the same order of magnitude (and often even **slightly** larger) than the corresponding differences between the SALSA and the MT versions of the aerosol transport model.

### 775 3.4 Ångström exponent

The Ångström exponent  $\alpha$  in a wavelength interval  $[\lambda_1, \lambda_2]$  is defined as

$$\alpha = -\frac{\log(\tau(\lambda_1)/\tau(\lambda_2))}{\log(\lambda_1/\lambda_2)}, \quad (2)$$

where  $\tau$  denotes the extinction optical depth. This quantity is often used for obtaining particle size information (usually, the smaller the particle size, the larger  $\alpha$ ). Table 7 shows values of  $\alpha$  for our different test cases computed with the three model versions in the wavelength interval 532–1064 nm. If we compare the columns labelled MT-CGS and SALSA-CGS, then we see that the mass-transport model consistently gives lower values of  $\alpha$ . This is related to the high values of  $r_{\text{eff}}$  in that model, which we noted earlier. On the other hand, if we compare the columns labelled MT-EXT and MT-CGS, then we see that the new optics model (CGS) predicts higher values of  $\alpha$  than the



**Table 7.** Ångström exponent in the wavelength region 532–1064 nm for the four different geographical locations, one summer (2007-06-22, 12:00) and one winter (2007-12-22, 12:00) event, and three model versions, MT-EXT, MT-CGS and Salsa-CGS.

		MT-EXT	MT-CGS	SALSA-CGS
Summer	Poland	$0.32 \times 10^0$	$0.12 \times 10^1$	$0.28 \times 10^1$
	North Sea	$0.80 \times 10^0$	$0.12 \times 10^1$	$0.21 \times 10^1$
	Northern Italy	$0.11 \times 10^1$	$0.11 \times 10^1$	$0.15 \times 10^1$
	Mediterranean	$0.36 \times 10^0$	$0.12 \times 10^1$	$0.21 \times 10^1$
Winter	Poland	$0.80 \times 10^0$	$0.12 \times 10^1$	$0.22 \times 10^1$
	North Sea	$0.79 \times 10^0$	$0.11 \times 10^1$	$0.14 \times 10^1$
	Northern Italy	$0.13 \times 10^1$	$0.10 \times 10^1$	$0.12 \times 10^1$
	Mediterranean	$0.13 \times 10^1$	$0.98 \times 10^0$	$0.14 \times 10^1$

785 old model (EXT) in ~~the first six rows, and lower values in the last two rows~~ June (summer) for all  
four geographical locations and in December (winter) for the locations Poland and North Sea. This  
indicates that the errors introduced by the simple external-mixture model in computing  $\alpha$  are quite  
unpredictable, even the sign of the error. When used in a size retrieval algorithm the retrieval errors  
caused by the EXT model would be equally hard to predict. The difference between the MT and  
790 SALSA model is somewhat larger, but not much larger, than the differences between the old and  
new optics models. Note that the performance of the MT model could be improved in comparison to  
SALSA by modifying the assumed size distribution in the MT model. By contrast, the differences  
between the two optics models ~~is~~ are rather fundamental; it is caused by the ~~over-simplified-simple~~  
treatment of aerosol morphology in the EXT model.

#### 795 4 Conclusions

We have implemented a new ~~aerosol-optics~~ aerosol-optics model in a regional chemical transport  
model. The new model differs from an earlier optics model described in Kahnert (2008) in three  
essential points. (i) While the old model treats all chemical components as externally mixed, the  
new model accommodates both external and internal mixtures of aerosol species. (ii) The old model  
800 treats black carbon ~~aerosols~~ particles as homogeneous spheres; the new model assumes a fractal ag-  
gregate morphology with fractal parameters based on observations. Mass absorption cross sections  
and single scattering albedos computed with this model have previously been evaluated by com-  
parison with measurements (Kahnert, 2010b). (iii) The new model describes internally mixed black  
carbon ~~aerosols~~ particles by a recently developed “core-grey-shell” model (Kahnert et al., 2013).  
805 This model accounts for the inhomogeneous internal mixing state of black carbon aggregates en-

capsulated in a shell of liquid-phase material. The model has been evaluated by comparison with reference computations based on observation-derived realistic models for encapsulated fractal aggregates (Kahnert et al., 2013). Item (i) has been incorporated in other CTMs earlier (e.g. Saide et al., 2013); however, to the best of our knowledge, items (ii) and (iii) go significantly beyond the  
810 current state-of-the-art of ~~aerosol-optics~~aerosol-optics models employed in CTMs. The main question of the present study is whether or not such a substantial level of detail in the description of aerosol morphology and optical properties is needed in a CTM.

~~To this end we compare radiative fluxes, backscattering coefficients, and Ångström exponents modelled with the old and new optics models~~We first performed a comparison of optical properties  
815 averaged over the entire model domain and over one month. To gauge the differences ~~we observe between~~the new and the old optics model, we further compare two model versions of the CTM with different levels of detail in the aerosol process descriptions, namely, one version that includes ~~aerosol dynamic~~aerosol-dynamic processes, and ~~one a~~a simpler mass-transport model, in which aerosol ~~dynamics-microphysics~~is switched off. The importance of aerosol ~~dynamics-microphysics~~is well  
820 understood and can therefore serve as a reference. ~~The comparison showed that both for radiative fluxes, and for backscattering coefficients, and for Ångström exponents the differences~~We found that the differences in optical properties between the two optics models are on the same order as those between the versions that include and exclude microphysical processes. For example, the aerosol optical depth computed with the two optics models differs by -25-18 %; differences obtained by  
825 inclusion or omission of aerosol microphysics are between -50-37 %. Corresponding differences in the backscattering coefficient are -8-99 % and -47-28 %, respectively. Analogous observations can be made for other radiometric properties.

We further wanted to understand how the differences in optical properties impact radiative transfer processes in an aerosol-laden atmosphere. To this end we compare radiative fluxes modelled with the  
830 old and new optics models. The comparison showed that the differences in radiative net-fluxes between the two ~~different~~optics models are of similar magnitude as corresponding differences between  
an aerosol dynamics and a the aerosol-microphysics and the mass-transport ~~model. This strongly suggests that over-simplified aerosol optics models are likely to~~models.

These results strongly suggest that simplifications in the assumptions on aerosol morphology in  
835 the optics model can introduce substantial errors in modelled radiative fluxes and ~~remote-sensing-relevant observables.~~In Earth-system-observables relevant to remote sensing. In chemistry-climate models such errors would enter into the simulation of the direct aerosol radiative forcing effect and add to all other sources of error in the model. In model evaluations that make use of remote sensing observations these errors would complicate the comparison between model results and observations.

840 The modifications to the ~~optics model studied here~~morphology-assumptions in the optics model were limited to ~~black carbon aerosols~~black-carbon particles. There are many other ~~aerosols~~aerosol particles with complex morphological properties, such as mineral dust, which our optics model

still treats by ~~an over-simplified homogeneous sphere~~ a simple homogeneous sphere model. The findings of our study should be an incentive for improving the description of dust and ~~volcanic ash~~ volcanic ash optical modelling in CTMs. A recent review of our current ~~state of knowledge~~ state of knowledge on aerosol morphology and aerosol optics for a variety of different ~~aerosols has recently been reviewed~~ aerosol particles can be found in Kahnert et al. (2014).

The findings of this study are likely to have implications for chemical data assimilation. In data assimilation one employs an *observation operator* that maps the model results to observable quantities. In case of satellite-based observations of aerosol optical properties, the observation operator is just our ~~aerosol optics~~ aerosol optics model, possibly coupled to a radiative transfer model. Many ~~data assimilation~~ data assimilation methodologies, such as the variational method, require a linear (or, at least, linearised) observation operator. In the old optics model, which assumes ~~externally mixed aerosols~~ externally-mixed aerosol particles, the observation operator is, indeed, linear (Kahnert, 2008). This largely explains why external-mixture optics models are widely used in chemical data assimilation systems (e.g. Kahnert, 2008; Benedetti et al., 2009; Liu et al., 2011). However, the new optics model we introduced here does not provide us with a linear map from the aerosol concentrations to the optical parameters. To what extent one could linearise this model and make use of its Jacobian in a data assimilation system mainly depends on the degree of nonlinearity, which would need to be investigated thoroughly.

~~All datasets used in this study, the MATCH model data and the aerosol optics data~~

## 5 Code availability

The aerosol microphysics code SALSA is distributed under the Apache 2.0 license, while the chemistry transport model MATCH and the aerosol-optics data base are available upon request ~~contacting the second author.~~ from SMHI.

## Appendix A: Size-averaged optical properties in the external-mixture optics model

The external-mixture optics model is based on using four size bins that cover the dry-radius intervals  $[r^{\min}, r^{\max}] = [0.01, 0.05] \mu\text{m}$ ,  $[0.05, 0.5] \mu\text{m}$ ,  $[0.5, 1.25] \mu\text{m}$ , and  $[1.25, 5] \mu\text{m}$ . The geometric mean radius  $R = \sqrt{r^{\min} r^{\max}} = 0.5(\log r^{\min} + \log r^{\max})$  is given in each of these intervals by  $R_1=0.022 \mu\text{m}$ ,  $R_2=0.158 \mu\text{m}$ ,  $R_3=0.791 \mu\text{m}$ , and  $R_4=2.5 \mu\text{m}$ . In each size bin it is assumed that the particle number density is given by a log-normal distribution

$$n_i(r) = N_i^0 / (\sqrt{2\pi} r \ln \sigma_i) \exp[-\ln^2(r/R_i)/(2\ln^2 \sigma_i)], \quad (\text{A1})$$

where  $\sigma_1 = \sigma_3 = \sigma_4 = 1.8$ ,  $\sigma_2 = 1.5$  are based on measurements in Neusüß et al. (2002). Here,  $N_i^0$  would be the total number density per mode if each size-mode extended from  $r = 0$  to  $r = \infty$ . However, since each mode is truncated at the bin-boundaries  $r^{\min}$  and  $r^{\max}$ , the number density  $N_i$

of particles per size bin is obtained from integration over this finite interval, i.e.

$$N_i = \int_{r_i^{\min}}^{r_i^{\max}} n_i(r) dr = N_i^0 \frac{1}{2} [\operatorname{erf}(x_i^{\max}) - \operatorname{erf}(x_i^{\min})], \quad (\text{A2})$$

where  $x_i^{\max} = \ln(r_i^{\max}/R_i)/(\sqrt{2}\ln\sigma_i)$ , and similarly for  $x_i^{\min}$ . Analogously, one obtains the particle-mass density  $M_i$  in each size bin by integrating over the truncated log-normal mode, which yields

$$\begin{aligned} 880 \quad M_i &\equiv \frac{4}{3}\pi\rho_i \int_{r_i^{\min}}^{r_i^{\max}} n_i(r)r^3 dr \\ &\equiv \frac{4}{3}\pi R_i^3 \rho_i N_i^0 \exp\left(\frac{9}{2}\ln^2\sigma_i\right) \frac{1}{2} [\operatorname{erf}(y_i^{\max}) - \operatorname{erf}(y_i^{\min})], \end{aligned} \quad (\text{A3})$$

where  $y_i^{\max} = x_i^{\max} - 3\ln\sigma_i/\sqrt{2}$ , and similarly for  $y_i^{\min}$ , and where  $\rho_i$  is the density of the aerosol particles in the  $i$ th size bin. From this we obtain the desired relation for converting the mass-density  $M_i$  into the number-density  $N_i$ :

$$885 \quad N_i = \frac{M_i}{\frac{4}{3}\pi R_i^3 \rho_i} \cdot \frac{\operatorname{erf}(x_i^{\max}) - \operatorname{erf}(x_i^{\min})}{\exp\left(\frac{9}{2}\ln^2\sigma_i\right) [\operatorname{erf}(y_i^{\max}) - \operatorname{erf}(y_i^{\min})]}. \quad (\text{A4})$$

Mass-mixing ratios  $X_i$  are simply converted into mass densities  $M_i$  according to  $M_i = X_i \rho_{\text{air}}$ , where  $\rho_{\text{air}}$  denotes the density of air.

In the external-mixture optics-database, optical properties are pre-computed by integrating optical properties at discrete sizes over the truncated log-normal size distribution. This integration is done numerically with a high size-resolution. The computation is performed for different refractive indices  $m$ , optical wavelengths  $\lambda$ , and for each size bin  $i$ . Thus, one obtains, e.g., extinction cross sections  $C_{\text{ext}}(\lambda, m, i)$ , which can be saved in a look-up table.

Secondary inorganic aerosols as well as organic aerosols and sea salt are assumed to be hydrophilic. We use the parameterisation by Gerber (1985) to compute the wet-radius  $r_w$  from the aerosol dry radius  $R$ , from which we obtain the volume-fraction of water  $f_w = (r_w^3 - R^3)/R^3$ . The effective refractive index  $m$  of the aerosol-water mixture is computed from that of the dry aerosol,  $m_a$ , and of water,  $m_w$  by use of effective-medium theory. In each grid cell, we obtain from the MATCH model, for each size bin  $i$  and for each aerosol component  $k$ , the number density  $N_i(k)$ . From that we compute the ensemble-averaged extinction cross section

$$900 \quad \bar{C}_{\text{ext}}(\lambda) = \frac{1}{N} \sum_k \sum_{i=1}^4 N_i(k) C_{\text{ext}}(\lambda, m(k), i), \quad (\text{A5})$$

where the total number density is given by

$$N = \sum_k \sum_{i=1}^4 N_i(k). \quad (\text{A6})$$

Note that the ensemble-average involves an average over both size and chemical composition. The ensemble-averaged scattering cross section  $\bar{C}_{\text{sca}}(\lambda)$  is computed analogously. From this we obtain

905 the averaged single-scattering albedo

$$\bar{\omega}(\lambda) = \frac{\bar{C}_{\text{sca}}(\lambda)}{\bar{C}_{\text{ext}}(\lambda)}. \quad (\text{A7})$$

The phase function  $p(\Theta)$ , hence its first Legendre-moment, known as the asymmetry parameter  $g$  are normalised quantities. Here  $\Theta$  denotes the scattering angle. To average these quantities, one first needs to "de-normalise" by multiplying them with the scattering cross section. Thus

$$910 \quad \bar{p}(\Theta; \lambda) \equiv \frac{1}{N\bar{C}_{\text{sca}}(\lambda)} \sum_k \sum_{i=1}^4 N_i(k) C_{\text{sca}}(\lambda, m(k), i) p(\Theta, m(k), i; \lambda) \quad (\text{A8})$$

$$\bar{g}(\lambda) \equiv \frac{1}{N\bar{C}_{\text{sca}}(\lambda)} \sum_k \sum_{i=1}^4 N_i(k) C_{\text{sca}}(\lambda, m(k), i) g(m(k), i; \lambda). \quad (\text{A9})$$

Once the ensemble-averaged optical properties in each grid cell of the model domain have been computed, one can compute radiometric observables, such as the extinction aerosol optical depth

$$\tau_{\text{ext}}(\lambda) = \sum_z N(z) \bar{C}_{\text{ext}}(\lambda, z) \Delta z, \quad (\text{A10})$$

915 or the backscattering coefficient

$$\beta_{\text{bak}}(\lambda, z) = \frac{1}{4\pi} N(z) \bar{C}_{\text{sca}}(\lambda, z) \bar{p}(180^\circ; \lambda, z), \quad (\text{A11})$$

where  $z$  labels grid cells in the vertical column, and  $\Delta z$  denotes the layer-thickness.

## Appendix B: Size-averaged optical properties in the internal-mixture model

In SALSA the number-density as a function of particle radius,  $n(r)$ , is given by a step-function with  
 920  $n_i(r) = \text{const}_i$  in each size bin  $i$ . This makes the pre-integration of optical properties over each size bin rather simple. On the other hand, we no longer assume that all aerosol components are externally mixed. Thus the ensemble-average over different chemical components  $k$  is no longer given by a simple summation  $\sum_k \dots$ , as it was in the external-mixture model. Rather, for each size bin in which  
 925 several aerosol components are internally mixed one computes an effective refractive index,  $m_{\text{eff}}$ , by use of effective-medium theory. One then reads the optical properties for that refractive index from the look-up table. Finally, one computes ensemble-averaged optical properties by summing over all size bins,  $\sum_i \dots$ .

## Appendix C: Effective-medium theory

930 In effective-medium theory (EMT) one considers a composite material consisting of two materials  
 with refractive indices  $m_1$  and  $m_2$  and volume fractions  $f_1$  and  $f_2 = 1 - f_1$ . One then invokes  
 assumptions about the topology of the mixture and derives a formula for the effective refractive  
 index,  $m_{\text{eff}}$ , of the composite material. For instance, it is often the case that  $f_1 \gg f_2$ . In this case  
 one can regard the first material as a host matrix that contains inclusions of the second material.  
 This is the basis of the Maxwell-Garnett EMT (Maxwell Garnett, 1904). The resulting expression  
 935 for  $m_{\text{eff}}$  is

$$m_{\text{eff}} = \sqrt{m_1^2 \frac{m_1^2(2 - 2f_2) + m_2^2(1 + 2f_2)}{m_1^2(2 + f_2) + m_2^2(1 - f_2)}}. \quad (\text{C1})$$

In the Bruggemann EMT (Bruggemann, 1935) one treats both materials more symmetrically; both  
 components are assumed to be embedded in a host matrix with an effective refractive index given by

$$940 \quad m_{\text{eff}} = \sqrt{\frac{1}{4}m_1^2(2 - 3f_2) + m_2^2(3f_2 - 1) + \sqrt{\frac{1}{16}[m_1^2(2 - 3f_2) + m_2^2(3f_2 - 1)]^2 + \frac{1}{2}m_1^2m_2^2}}. \quad (\text{C2})$$

Although not immediately manifest, this equation is symmetric under exchange of the two materials.

The volume-fraction is obtained from the mass concentrations  $M_1$  and  $M_2$  computed in the  
 transport model, i.e.  $f_2 = M_2/(M_1 + M_2)$ . In SALSA, we apply the Maxwell-Garnett rule for an  
 945 internal mixtures of mineral-dust inclusions in a host matrix of soluble compounds. Also, in the  
 core-grey-shell model the effective refractive index of the grey shell, i.e., the homogeneous mixture  
 of black carbon with soluble compounds, is computed with Maxwell-Garnett EMT. For mixtures of  
 soluble compounds (sulphate, nitrate, ammonium, sea salt, organic compounds, and water) we use  
 the Bruggemann EMT. If more than two components are mixed with each other, then the mixing rule  
 950 is applied iteratively.

#### Appendix D: Refractive indices

The refractive indices that are used in the new optics model (and in the effective-medium calculations)  
 are listed in Table 8.

#### Appendix E: Optical properties at different wavelengths in the considered case-studies

955 Figures 12–35 show vertical profiles of AOD, single-scattering albedo, and asymmetry parameter  
 at the four geographic location, for the summer and winter incident, and for 12 different optical  
 wavelengths.

**Table 8.** Refractive index  $m$  for each wavelength in the aerosol-optics look-up table and for various aerosol components.

$\lambda$ [ $\mu\text{m}$ ]	0.2000	0.2316	0.3040	0.3400
$m(\text{SO}_4)$	1.4840+0.1000E-07 i	1.4840+0.1000E-07 i	1.4676+0.1000E-07 i	1.4554+0.1000E-07 i
$m(\text{BC})$	0.9400+0.3500E+00 i	1.0717+0.5817E+00 i	1.3314+0.7523E+00 i	1.4471+0.7214E+00 i
$m(\text{OC})$	1.5300+0.5000E-02 i	1.5300+0.5000E-02 i	1.5300+0.5000E-02 i	1.5300+0.5000E-02 i
$m(\text{NaCl})$	1.5100+0.5000E-05 i	1.5100+0.5000E-05 i	1.5100+0.1866E-05 i	1.5100+0.6592E-06 i
$m(\text{Dust})$	1.5190+0.2070E-01 i	1.5190+0.2070E-01 i	1.5240+0.1947E-01 i	1.5272+0.1683E-01 i
$m(\text{H}_2\text{O})$	1.4517+0.1101E-06 i	1.4094+0.1092E-07 i	1.3701+0.3879E-08 i	1.3604+0.2758E-08 i
$\lambda$ [ $\mu\text{m}$ ]	0.3550	0.3800	0.3932	0.4400
$m(\text{SO}_4)$	1.4508+0.1000E-07 i	1.4448+0.1000E-07 i	1.4416+0.1000E-07 i	1.4336+0.1000E-07 i
$m(\text{BC})$	1.4954+0.7086E+00 i	1.5757+0.6871E+00 i	1.6181+0.6758E+00 i	1.6771+0.6586E+00 i
$m(\text{OC})$	1.5300+0.5000E-02 i	1.5300+0.5000E-02 i	1.5300+0.5000E-02 i	1.5300+0.5000E-02 i
$m(\text{NaCl})$	1.5090+0.2946E-06 i	1.5040+0.1476E-06 i	1.5014+0.6998E-07 i	1.5000+0.2544E-07 i
$m(\text{Dust})$	1.5239+0.1250E-01 i	1.5160+0.2500E-02 i	1.5147+0.2170E-02 i	1.5135+0.1400E-02 i
$m(\text{H}_2\text{O})$	1.3572+0.2416E-08 i	1.3528+0.1944E-08 i	1.3508+0.1702E-08 i	1.3449+0.9324E-09 i
$\lambda$ [ $\mu\text{m}$ ]	0.5000	0.5320	0.5332	0.6750
$m(\text{SO}_4)$	1.4310+0.1000E-07 i	1.4304+0.1000E-07 i	1.4303+0.1000E-07 i	1.4285+0.1860E-07 i
$m(\text{BC})$	1.7329+0.6414E+00 i	1.7626+0.6323E+00 i	1.7637+0.6319E+00 i	1.8097+0.5824E+00 i
$m(\text{OC})$	1.5300+0.5000E-02 i	1.5300+0.5000E-02 i	1.5300+0.5000E-02 i	1.5300+0.7091E-02 i
$m(\text{NaCl})$	1.5000+0.1550E-07 i	1.5000+0.1198E-07 i	1.5000+0.1185E-07 i	1.4900+0.1212E-06 i
$m(\text{Dust})$	1.5160+0.1200E-02 i	1.5167+0.1129E-02 i	1.5167+0.1126E-02 i	1.5170+0.9818E-03 i
$m(\text{H}_2\text{O})$	1.3394+0.9243E-09 i	1.3371+0.1818E-08 i	1.3370+0.1850E-08 i	1.3297+0.2187E-07 i
$\lambda$ [ $\mu\text{m}$ ]	0.7016	0.8700	1.0101	1.0200
$m(\text{SO}_4)$	1.4280+0.2214E-07 i	1.4253+0.2044E-06 i	1.4216+0.1749E-05 i	1.4213+0.1963E-05 i
$m(\text{BC})$	1.8175+0.5730E+00 i	1.8752+0.5645E+00 i	1.9210+0.5622E+00 i	1.9219+0.5643E+00 i
$m(\text{OC})$	1.5300+0.7333E-02 i	1.5300+0.9409E-02 i	1.5300+0.1327E-01 i	1.5300+0.1370E-01 i
$m(\text{NaCl})$	1.4900+0.2282E-06 i	1.4800+0.3027E-04 i	1.4700+0.1498E-03 i	1.4700+0.1584E-03 i
$m(\text{Dust})$	1.5170+0.9335E-03 i	1.5184+0.8000E-03 i	1.5190+0.7347E-03 i	1.5190+0.7261E-03 i
$m(\text{H}_2\text{O})$	1.3287+0.3624E-07 i	1.3243+0.3714E-06 i	1.3215+0.2657E-05 i	1.3213+0.2380E-05 i
$\lambda$ [ $\mu\text{m}$ ]	1.0640	1.2705	1.4625	1.7840
$m(\text{SO}_4)$	1.4197+0.2915E-05 i	1.4122+0.1621E-04 i	1.4045+0.1030E-03 i	1.3926+0.5308E-03 i
$m(\text{BC})$	1.9261+0.5738E+00 i	1.9457+0.6183E+00 i	1.9639+0.6597E+00 i	1.9943+0.7290E+00 i
$m(\text{OC})$	1.5285+0.1515E-01 i	1.5179+0.1721E-01 i	1.5068+0.1864E-01 i	1.4801+0.1337E-01 i
$m(\text{NaCl})$	1.4700+0.1966E-03 i	1.4692+0.3754E-03 i	1.4615+0.5382E-03 i	1.4500+0.7944E-03 i
$m(\text{Dust})$	1.5190+0.6853E-03 i	1.5188+0.6418E-03 i	1.5180+0.8000E-03 i	1.5180+0.9990E-03 i
$m(\text{H}_2\text{O})$	1.3205+0.1279E-05 i	1.3167+0.1090E-04 i	1.3128+0.3528E-03 i	1.3040+0.1270E-03 i
$\lambda$ [ $\mu\text{m}$ ]	2.0460	2.3250	2.7885	3.4615
$m(\text{SO}_4)$	1.3803+0.1490E-02 i	1.3580+0.2885E-02 i	1.3146+0.5669E-01 i	1.3669+0.1579E+00 i
$m(\text{BC})$	2.0192+0.7854E+00 i	2.0510+0.8453E+00 i	2.1099+0.9444E+00 i	2.1955+0.1088E+01 i
$m(\text{OC})$	1.4613+0.1000E-01 i	1.4554+0.9641E-02 i	1.4800+0.7724E-02 i	1.4800+0.7000E-02 i
$m(\text{NaCl})$	1.4482+0.1276E-02 i	1.4370+0.2950E-02 i	1.5339+0.7462E-02 i	1.4800+0.1757E-02 i
$m(\text{Dust})$	1.5180+0.1492E-02 i	1.5180+0.2610E-02 i	1.5180+0.8077E-02 i	1.5180+0.2805E-01 i
$m(\text{H}_2\text{O})$	1.2947+0.7103E-03 i	1.2756+0.5344E-03 i	1.1278+0.1055E+00 i	1.3913+0.1237E-01 i
$\lambda$ [ $\mu\text{m}$ ]	3.5000	8.0205	10.6000	12.1950
$m(\text{SO}_4)$	1.3760+0.1580E+00 i	1.1641+0.5511E+00 i	1.7200+0.3400E+00 i	1.7858+0.2517E+00 i
$m(\text{BC})$	2.2004+0.1097E+01 i	2.6572+0.1742E+01 i	2.9285+0.2063E+01 i	3.0719+0.2210E+01 i
$m(\text{OC})$	1.4800+0.7000E-02 i	1.1237+0.7906E-01 i	1.7600+0.7000E-01 i	1.6352+0.5117E-01 i
$m(\text{NaCl})$	1.4800+0.1600E-02 i	1.4080+0.1581E-01 i	1.5000+0.1400E-01 i	1.4383+0.1539E-01 i
$m(\text{Dust})$	1.5180+0.2973E-01 i	1.1798+0.1015E+00 i	1.9100+0.2500E+00 i	1.7614+0.4543E+00 i
$m(\text{H}_2\text{O})$	1.3840+0.9340E-02 i	1.2676+0.3436E-01 i	1.1531+0.7145E-01 i	1.0874+0.2243E+00 i

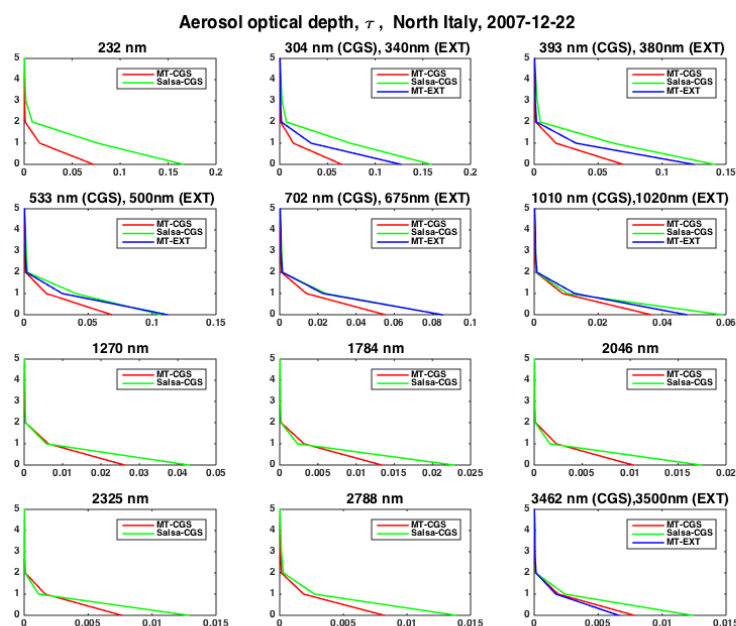


**Figure 12.** Aerosol optical depth over North Italy at 22-12-2007 for the 12 wavelengths in the CGS optics model and 5 of the 7 wavelengths in the EXT model. The wavelengths do not exactly overlap, but the EXT wavelengths that lies within 40 nm of the CGS wavelength are plotted in the same graph.

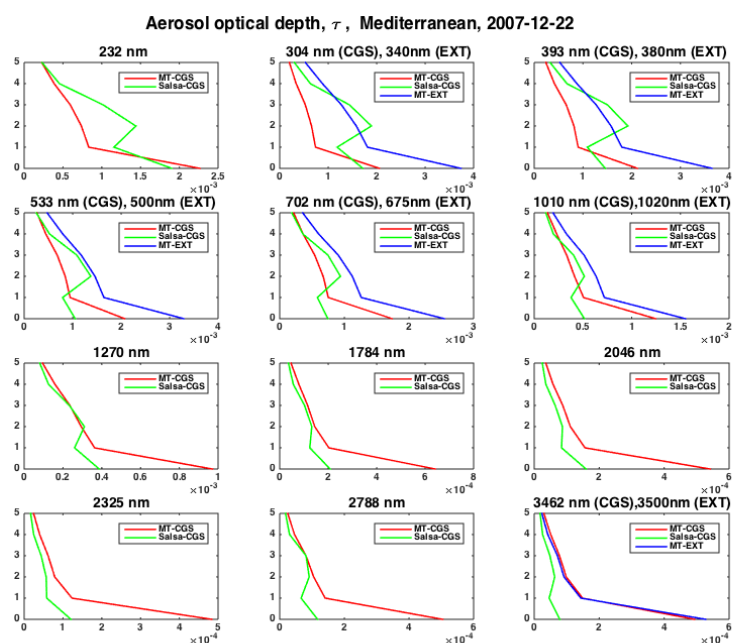


**Figure 13.** Same as Fig. 12, but over the Mediterranean.



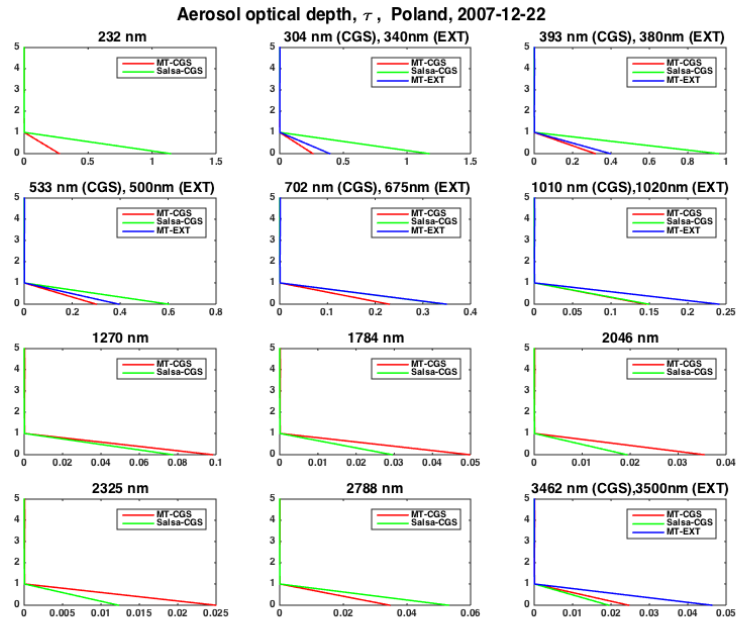


Figure 14. Same as Fig. 12, but over Poland.

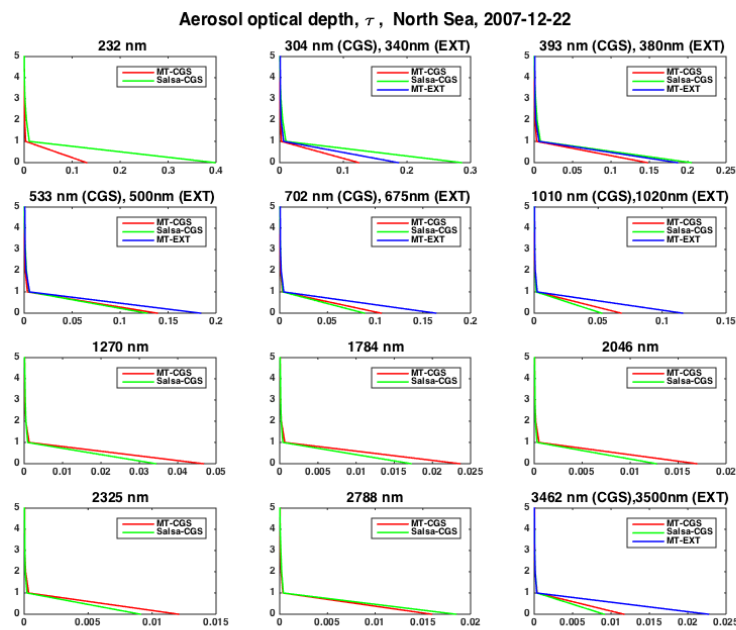


Figure 15. Same as Fig. 12, but over the North Sea

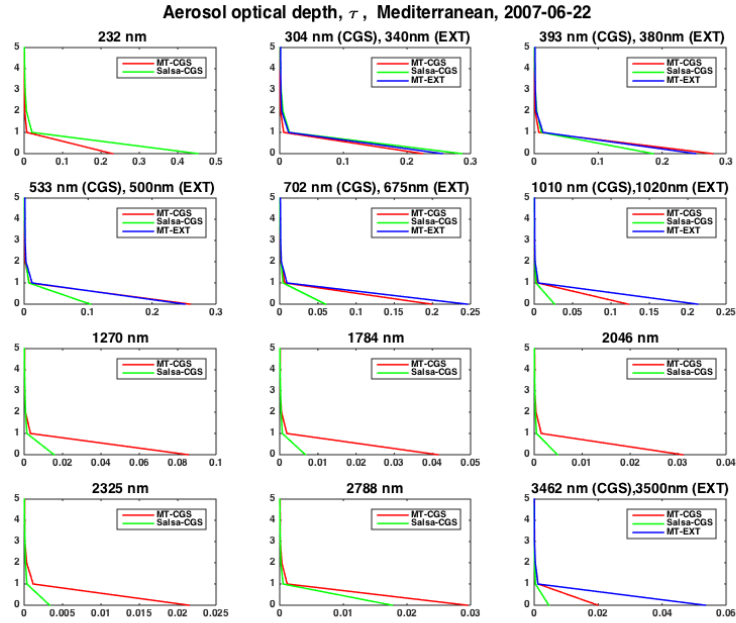


Figure 16. Same as Fig. 12, but 2007-06-22.

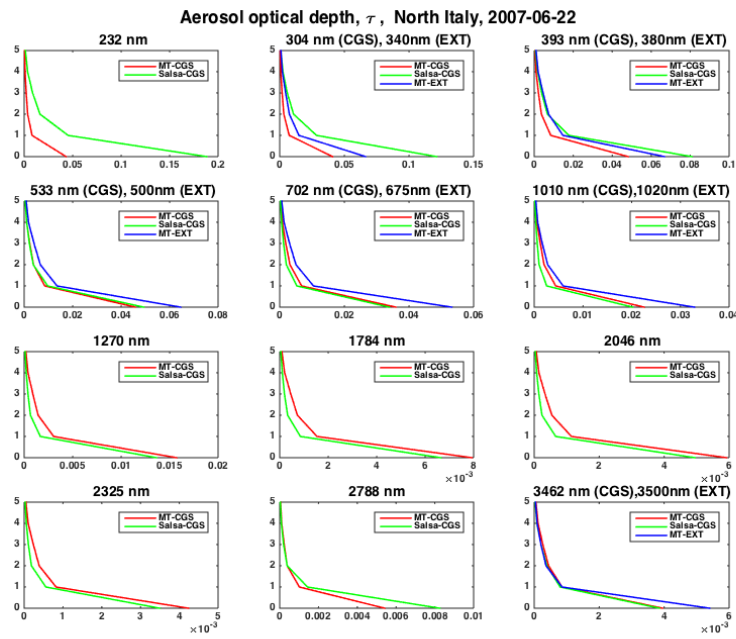


Figure 17. Same as Fig. 12, but 2007-06-22 and over the Mediterranean.

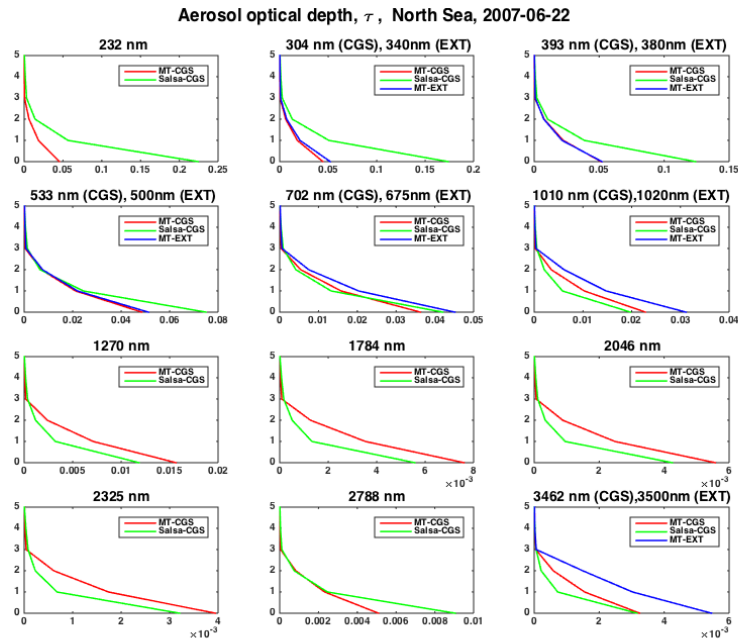


Figure 18. Same as Fig. 12, but 2007-06-22 and over Poland.

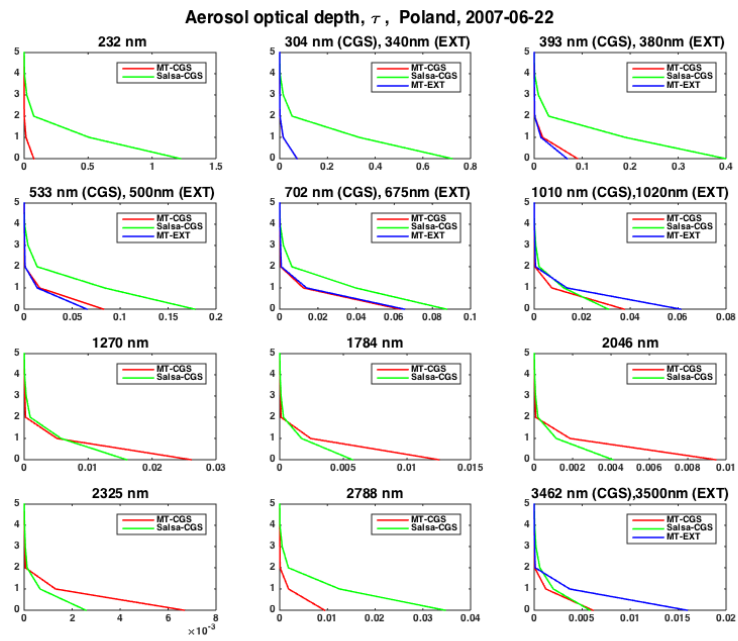
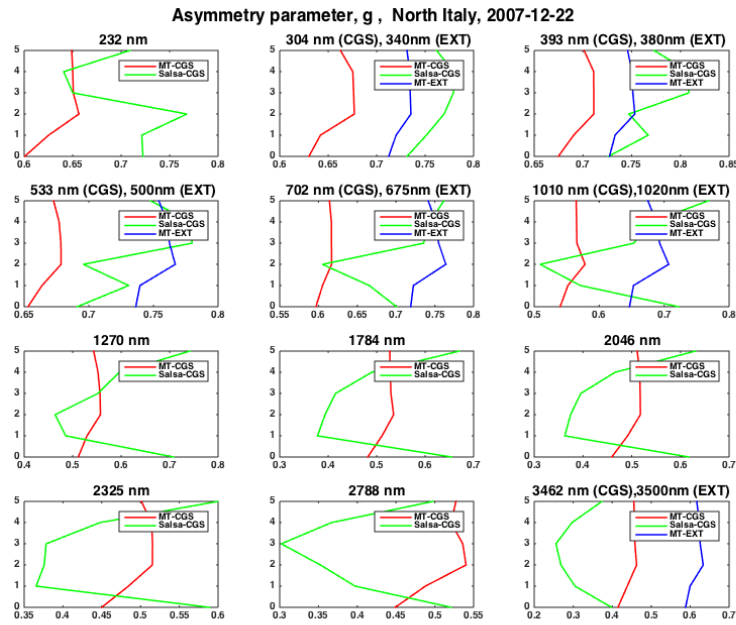
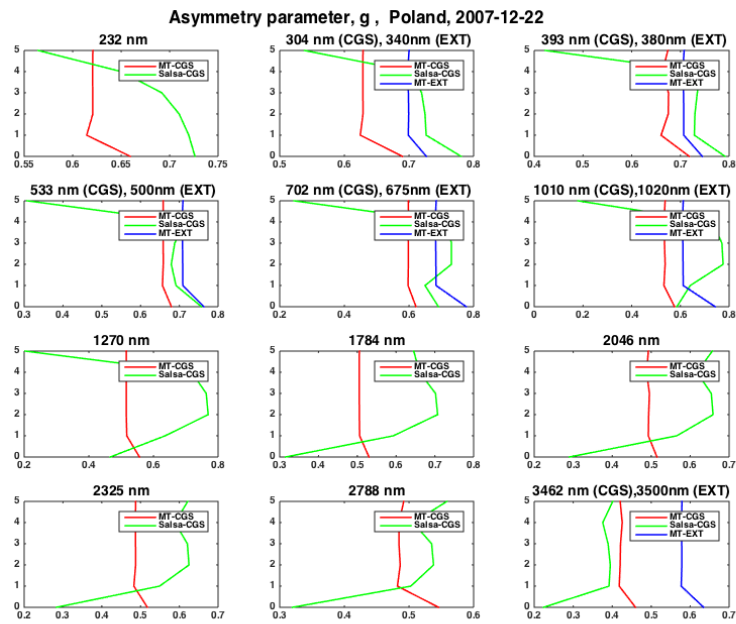


Figure 19. Same as Fig. 12, but 2007-06-22 and over the North sea.



**Figure 20.** Asymmetry parameter over North Italy at 22-12-2007 for the 12 wavelengths in the CGS optics model and 5 of the 7 wavelengths in the EXT model. The wavelengths do not exactly overlap, but the EXT wavelengths that lies within 40 nm of the CGS wavelength are plotted in the same graph.



**Figure 21.** Same as Fig. 20, but over the Mediterranean.

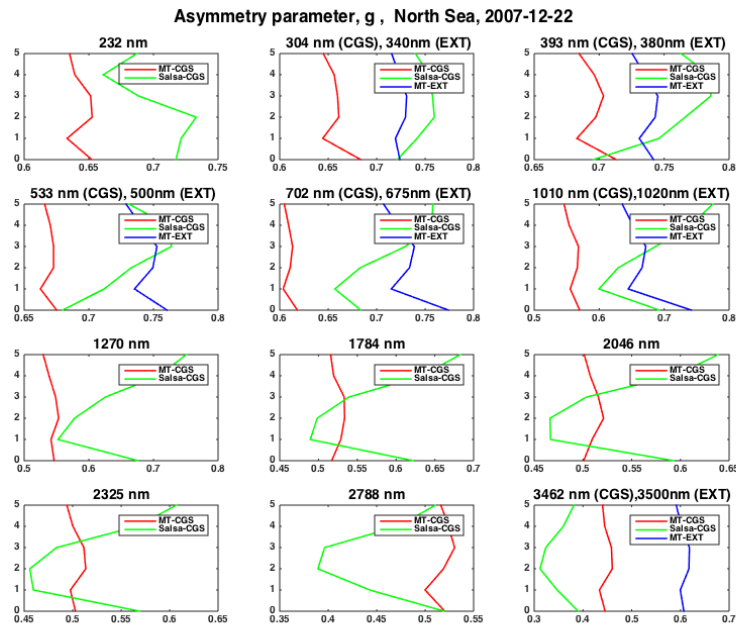


Figure 22. Same as Fig. 20, but over Poland.

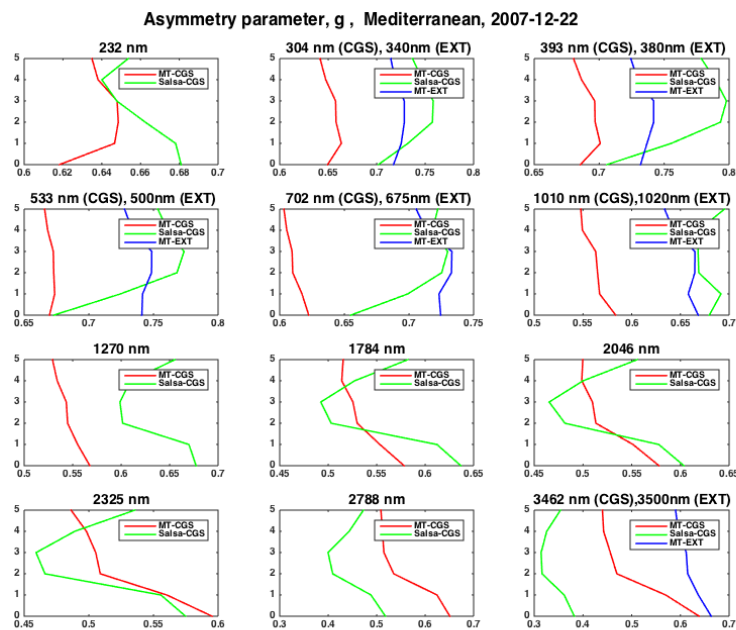


Figure 23. Same as Fig. 20, but over the North sea.

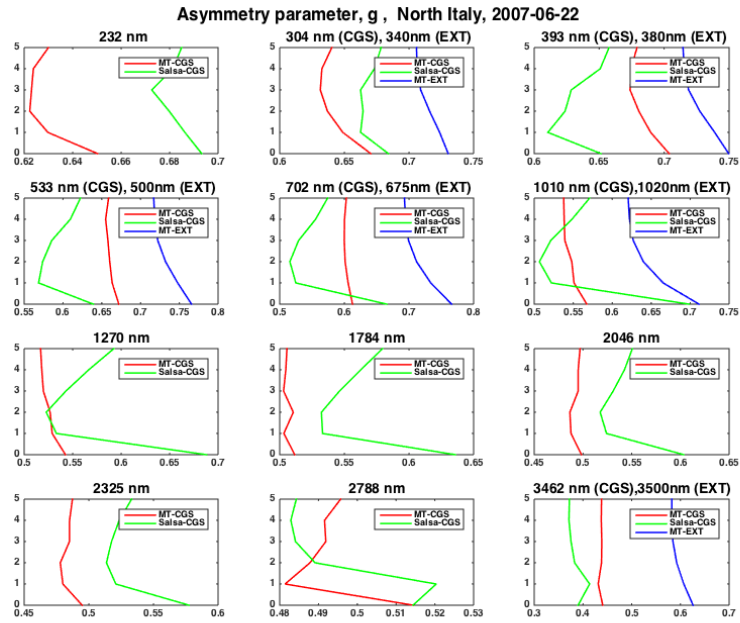


Figure 24. Same as Fig. 20, but 2007-06-22.

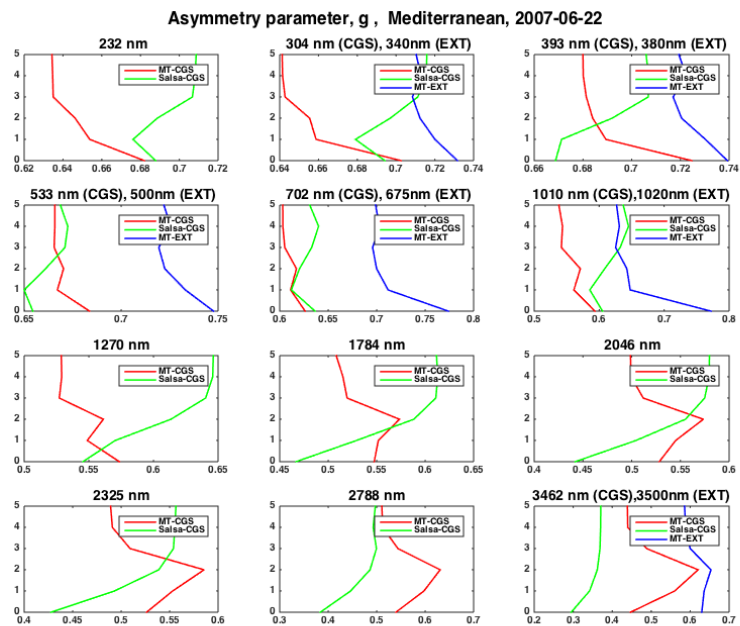


Figure 25. Same as Fig. 20, but 2007-06-22 and over the Mediterranean.

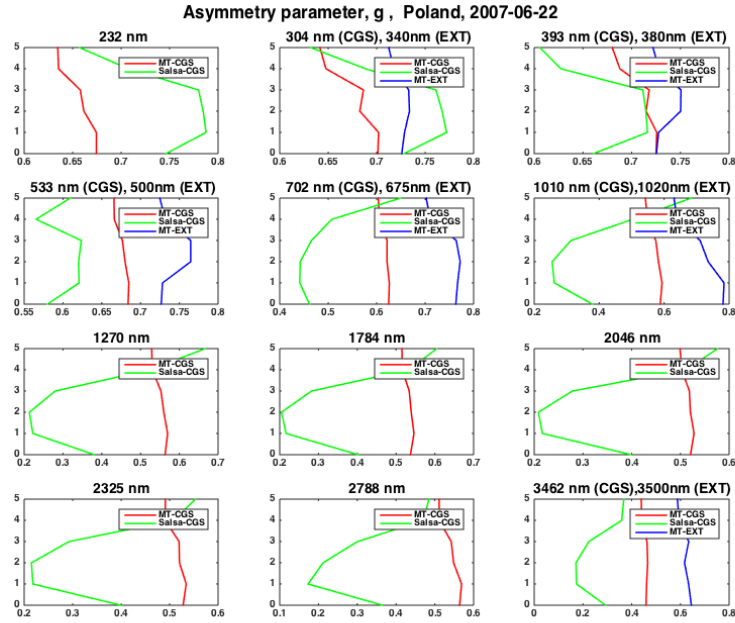


Figure 26. Same as Fig. 20, but 2007-06-22 and over Poland.

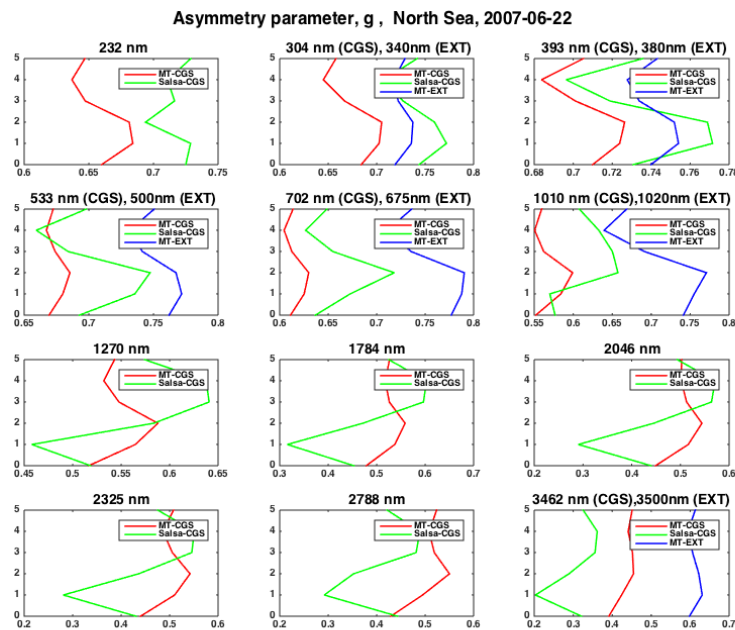
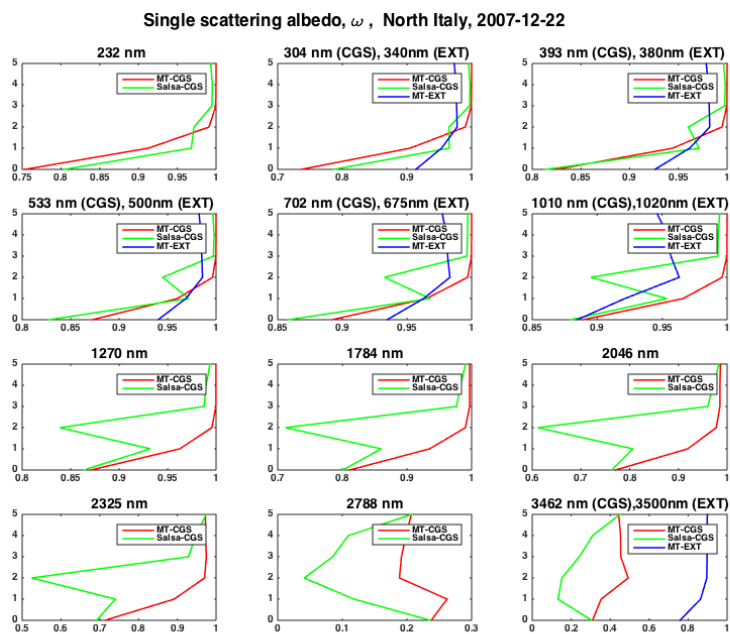
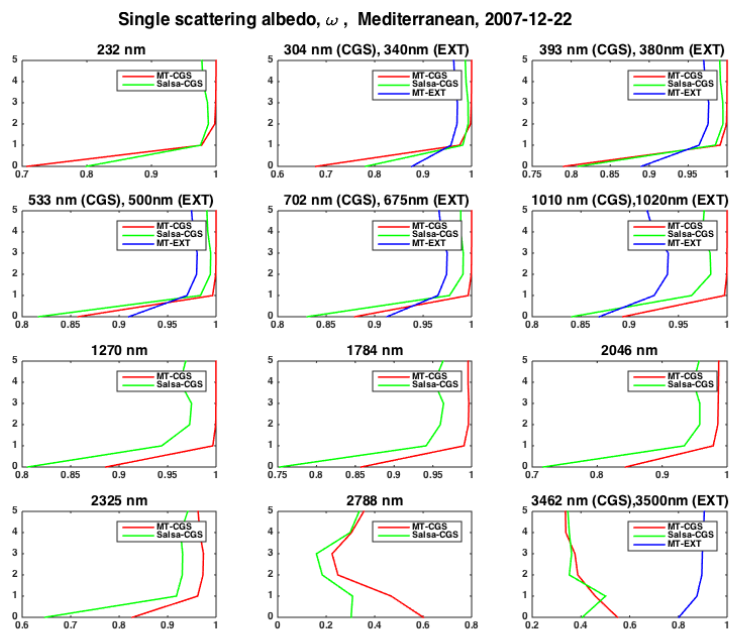


Figure 27. Same as Fig. 20, but 2007-06-22 and over the North sea.



**Figure 28.** Single scattering albedo over North Italy at 22-12-2007 for the 12 wavelengths in the CGS optics model and 5 of the 7 wavelengths in the EXT model. The wavelengths do not exactly overlap, but the EXT wavelengths that lies within 40 nm of the CGS wavelength are plotted in the same graph.



**Figure 29.** Same as Fig. 28, but over the Mediterranean.



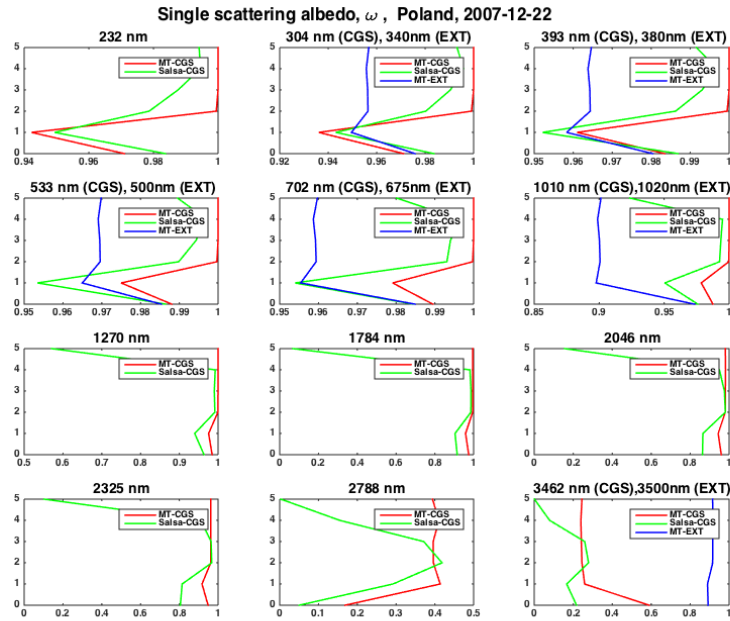


Figure 30. Same as Fig. 28, but over Poland.

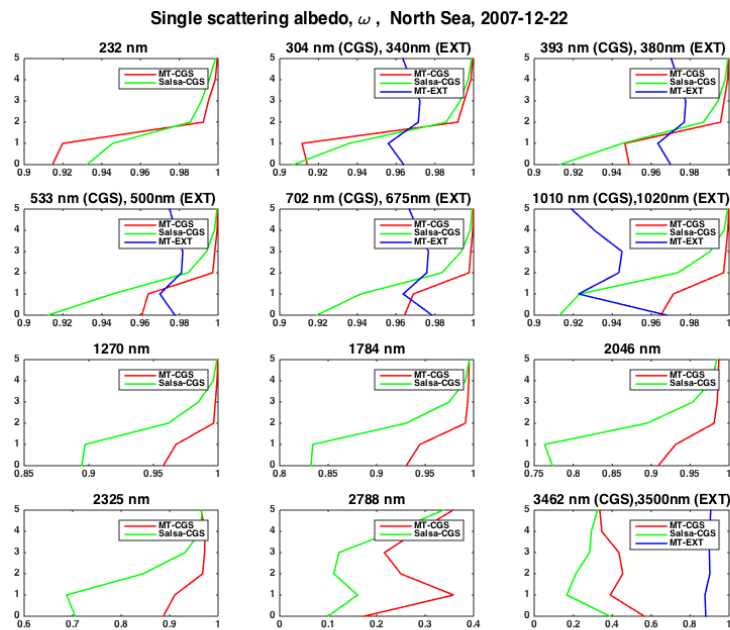


Figure 31. Same as Fig. 28, but over the North sea.

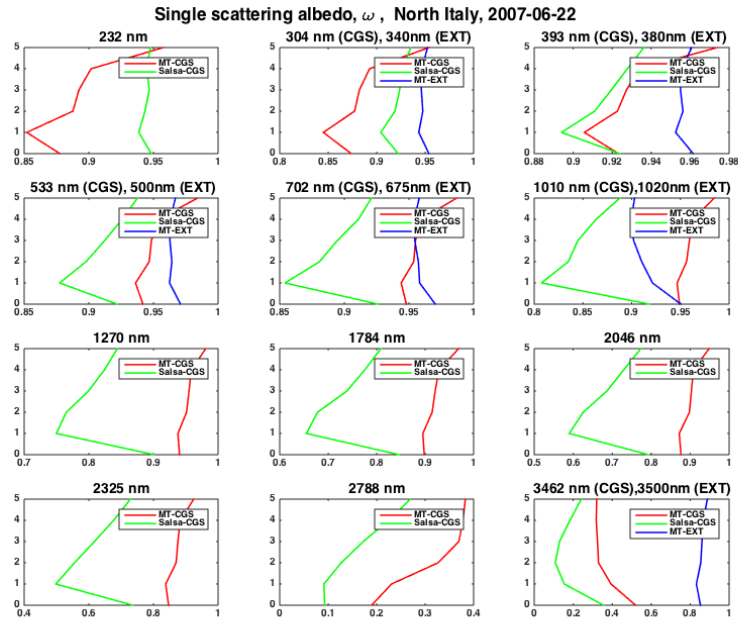


Figure 32. Same as Fig. 28, but 2007-06-22.

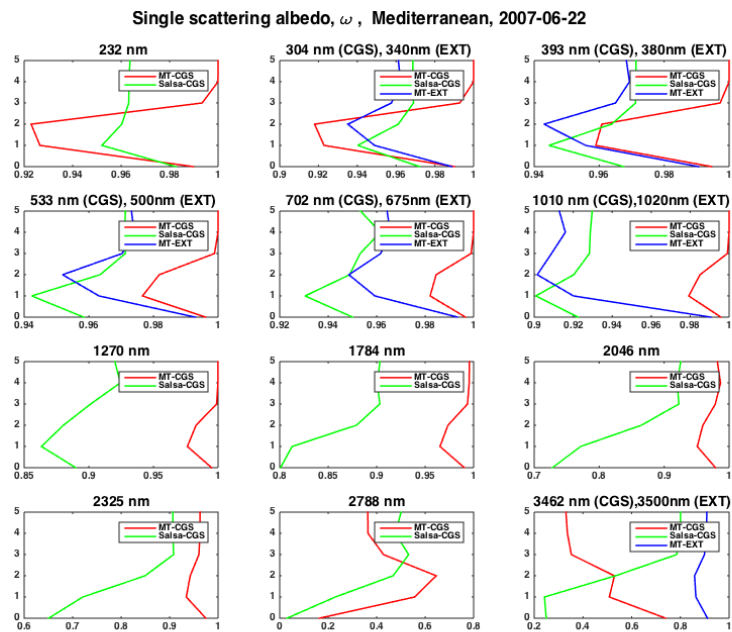


Figure 33. Same as Fig. 28, but 2007-06-22 and over the Mediterranean.

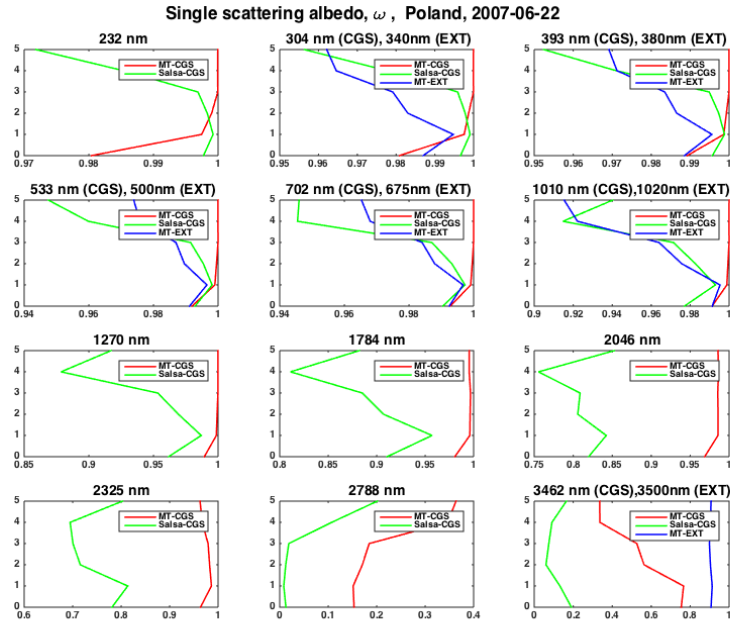


Figure 34. Same as Fig. 28, but 2007-06-22 and over Poland.

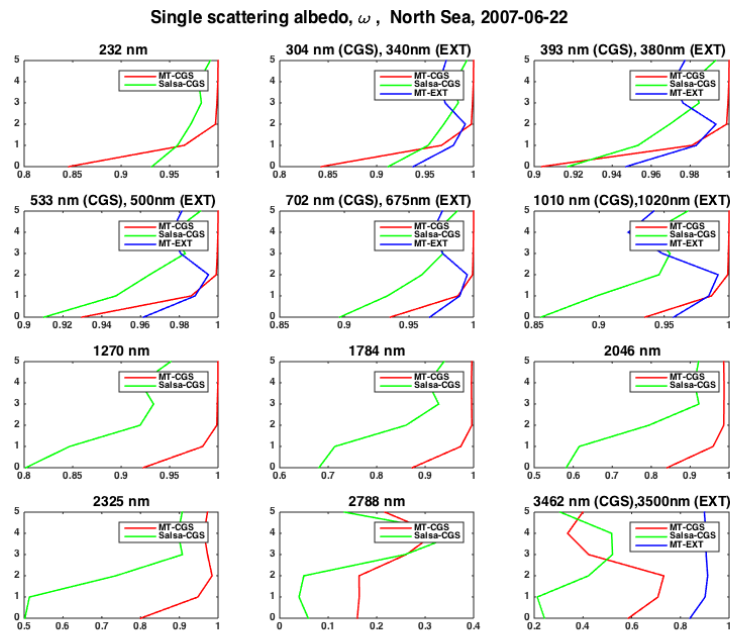


Figure 35. Same as Fig. 28, but 2007-06-22 and over the North sea.

*Acknowledgements.* E. Andersson acknowledge funding from the Swedish National Space Board within the OSCES project (No. 101/13). M. Kahnert has been funded by the Swedish Research Council (Vetenskapsrådet) 960 within the AGES project (project 621-2011-3346).

## References

- Adachi, K. and Buseck, P. R.: Internally mixed soot, sulfates, and organic matter in aerosol particles from Mexico City, *Atmos. Chem. Phys.*, 8, 6469–6481, doi:10.5194/acp-8-6469-2008, 2008.
- Adachi, K., Chung, S. H., Friedrich, H., and Buseck, P. R.: Fractal parameters of individual soot particles determined using electron tomography: Implications for optical properties, *J. Geophys. Res.*, 112, D14202, doi:10.1029/2006JD008296, 2007.
- 965
- Andersson, C., Langner, J., and Bergström, R.: Interannual variation and trends in air pollution over Europe due to climate variability during 1958–2001 simulated with a regional CTM coupled to the ERA40 reanalysis, *Tellus B*, 59, 77–98, 2007.
- 970 [Andersson, C., Bergström, R., Bennet, C., Thomas, M., Robertson, L., Kokkola, H., Korhonen, H., and Lehtinen, K.: MATCH-SALSA - Multi-scale Atmospheric Transport and Chemistry model coupled to the SALSA aerosol microphysics model, SMHI Report RMK 115, available at: <http://www.smhi.se/publikationer/match-salsa-multi-scale-atmospheric-transport-and-chemistry-model-coupled-to-the-salsa-aerosol-microphysics> \(last accessed 10 February 2016\), 2013.](#)
- 975 Andersson, C., Bergström, R., Bennet, C., Robertson, L., Thomas, M., Korhonen, H., Lehtinen, K. E. J., and Kokkola, H.: MATCH-SALSA – Multi-scale Atmospheric Transport and CHEMISTRY model coupled to the SALSA aerosol microphysics model – Part 1: Model description and evaluation, *Geosci. Model Dev.*, 8, 171–189, doi:10.5194/gmd-8-171-2015, 2015.
- Benedetti, A., Morcrette, M. J.-J., Boucher, O., Dethof, A., Engelen, R. J., Huneeus, M. F. H. F. N., Jones, L., and S. Kinne, J. W. K., Mangold, A., Razinger, M., Simmons, A. J., and Suttie, M.: Aerosol analysis and forecast in the European Centre for Medium-Range Weather Forecasts Integrated Forecast System: 2. Data assimilation, *J. Geophys. Res.*, 114, D13205, doi:10.1029/2008JD011115, 2009.
- 980
- Bond, T. C. and Bergstrom, R. W.: Light absorption by carbonaceous particles: An investigative review, *Aerosol Sci. Tech.*, 40, 27–67, 2006.
- 985 Bruggemann, D. A. G.: Berechnung verschiedener physikalischer Konstanten von heterogenen Substanzen. 1. Dielektrizitätskonstanten und Leitfähigkeiten der Mischkörper aus isotropen Substanzen, *Ann. Phys.-Berlin*, 24, 636–664, 1935.
- [China, S., Salvadori, N. and Mazzoleni, C.: Effect of Traffic and Driving Characteristics on Morphology of Atmospheric Soot Particles at Freeway On-Ramps, \*Environ. Sci. Technol.\*, 48 \(6\), 3128–3135, doi:10.1021/es405178n, 2014.](#)
- 990 [Chakrabarty, R.K., Beres, N.D., Moosmüller, H., China, S., Mazzoleni, C., Dubey, M.K., Liu, L., and Mishchenko, M.I.: Soot superaggregates from flaming wildfires and their direct radiative forcing, \*Scientific Reports\*, 4, 5508 EP, doi:10.1038/srep05508, 2014.](#)
- Chang, H. and Charalampopoulos, T. T.: Determination of the wavelength dependence of refractive indices of flame soot, *P. R. Soc. A*, 430, 577–591, 1990.
- 995 Dubovik, O., Sinyuk, A., Lapyonok, T., Holben, B. N., Mishchenko, M. I., Yang, P., Eck, T. F., Volten, H., Muñoz, O., Veihelmann, B., van der Zande, W. J., Leon, J.-F., Sorokin, M., and Slutsker, I.: Application of spheroid models to account for aerosol particle nonsphericity in remote sensing of desert dust, *J. Geophys. Res.*, 111, D11208, doi:10.1029/2005JD006619, 2006.

- 1000 Foltescu, V., Pryor, S. C., and Bennet, C.: Sea salt generation, dispersion and removal on the regional scale, *Atmos. Environ.*, 39, 2123–2133, 2005.
- Gerber, H. E.: Relative-humidity parameterization of the Navy Aerosol Model (NAM), Tech. Rep. 8956, Naval Research Laboratory, Washington, DC, 1985.
- 1005 [Jacobson, M. Z.: A physically-based treatment of elemental carbon optics: Implications for global direct forcing of aerosols, \*Geophys. Res. Lett.\*, 27, 217-220, 2000.](#)
- Jones, A. R.: Light scattering in combustion, in: *Light Scattering Reviews*, edited by: Kokhanovsky, A., Springer, Berlin, 393–444, 2006.
- Kahnert, F. M.: Reproducing the optical properties of fine desert dust aerosols using ensembles of simple model particles, *J. Quant. Spectrosc. Ra.*, 85, 231–249, 2004.
- 1010 Kahnert, M.: Variational data analysis of aerosol species in a regional CTM: background error covariance constraint and aerosol optical observation operators, *Tellus B*, 60, 753–770, 2008.
- Kahnert, M.: Modelling the optical and radiative properties of freshly emitted light absorbing carbon within an atmospheric chemical transport model, *Atmos. Chem. Phys.*, 10, 1403–1416, doi:10.5194/acp-10-1403-2010, 2010a.
- 1015 Kahnert, M.: On the discrepancy between modelled and measured mass absorption cross sections of light absorbing carbon aerosols, *Aerosol Sci. Tech.*, 44, 453–460, 2010b.
- Kahnert, M. and Devasthale, A.: Black carbon fractal morphology and short-wave radiative impact: a modelling study, *Atmos. Chem. Phys.*, 11, 11745–11759, doi:10.5194/acp-11-11745-2011, 2011.
- Kahnert, M., ~~Nousainen~~[Nousiainen](#), T., and Lindqvist, H.: Models for integrated and differential scattering optical properties of encapsulated light absorbing carbon aggregates, *Opt. Express*, 21, 7974–7993, 2013.
- 1020 Kahnert, M., Nousiainen, T., and Lindqvist, H.: Review: Model particles in atmospheric optics, *J. Quant. Spectrosc. Ra.*, 146, 41–58, 2014.
- [Khlebtsov, N. G.: Orientational averaging of light-scattering observables in the T-matrix approach, \*Appl. Opt.\*, 31, 5359-5365, 1992.](#)
- 1025 [Klingmüller, K., Steil, B., Brühl, C., Tost, H., and Lelieveld, J.: Sensitivity of aerosol radiative effects to different mixing assumptions in the AEROPT 1.0 submodel of the EMAC atmospheric-chemistry-climate model, \*Geosci. Model Dev.\*, 7, 2503–2516, doi:10.5194/gmd-7-2503-2014, 2014.](#)
- Kokkola, H., Korhonen, H., Lehtinen, K. E. J., Makkonen, R., Asmi, A., Järvenoja, S., Anttila, T., Partanen, A.-I., Kulmala, M., Järvinen, H., Laaksonen, A., and Kerminen, V.-M.: SALSA – a Sectional Aerosol module for Large Scale Applications, *Atmos. Chem. Phys.*, 8, 2469–2483, doi:10.5194/acp-8-2469-2008, 2008.
- 1030 Kupiainen, K. and Klimont, Z.: Primary emissions of submicron and carbonaceous particles in Europe and the potential for their control, Tech. Rep. IR-04-079, IIASA, Laxenburg, Austria, 2004.
- Kupiainen, K. and Klimont, Z.: Primary emissions of fine carbonaceous particles in Europe, *Atmos. Environ.*, 41, 2156–2170, 2007.
- 1035 Kylling, A., Bais, A. F., Blumthaler, M., Schreder, J., Zerefos, C. S., and Kosmidis, E.: The effect of aerosols on solar UV irradiances during the photochemical activity and solar ultraviolet radiation campaign, *J. Geophys. Res.*, 103, 26051–26060, 1998.

- Liu, Z., Liu, Q., Lin, H.-C., Schwartz, C. S., Lee, Y.-H., and Wang, T.: Three-dimensional variational assimilation of MODIS aerosol optical depth: Implementation and application to a dust storm over East Asia, *J. Geophys. Res.*, 116, D23206, doi:10.1029/2011JD016159, 2011.
- 1040 Mackowski, D. W. and Mishchenko, M. I.: A multiple sphere T-matrix Fortran code for use on parallel computer clusters, *J. Quant. Spectrosc. Ra.*, 112, 2182–2192, 2011.
- Mårtensson, E. M., Nilsson, E. D., de Leeuw, G., Cohen, L. H., and Hansson, H.-C.: Laboratory simulations and parameterization of the primary marine aerosol production, *J. Geophys. Res.*, 108, 4297, doi:10.1029/2002JD002263, 2003.
- 1045 [Matsui, H., Koike, M., Kondo, Y., Moteki, N., Fast, J.D., and Zaveri, R.A.: Development and validation of a black carbon mixing state resolved three-dimensional model: Ageing processes and radiative impact, \*J. Geophys. Res.\*, 118, 2304–2326, doi:10.1029/2012JD018446, 2013.](#)
- Maxwell Garnett, J. C.: Colours in metal glasses and in metallic films, *Philos. T. R. Soc. A*, 203, 385–420, 1904.
- 1050 Mishchenko, M. I., Travis, L. D., and Lacis, A. A.: Scattering, Absorption, and Emission of Light by Small Particles, Cambridge University Press, Cambridge, 2002.
- Monahan, E. C., Spiel, D. E., and Davidson, K. L.: A model of marine aerosol generation via whitecaps and wave disruption, in: *Oceanic Whitecaps and their Role in Air-Sea Exchange*, edited by: Monahan, E. C. and Niocaill, G. M., D Reidel, Norwell, MA, 167–174, 1986.
- 1055 Neusüß, C., Wex, H., Birmili, W., Wiedensohler, A., Koziar, C., Busch, B., Brüggemann, E., Gnauk, T., Ebert, M., and Covert, D. S.: Characterization and parameterization of atmospheric particle number-, mass-, and chemical-size distributions in central Europe during LACE 98 and MINT, *J. Geophys. Res.*, 107, LAC 9-1–LAC 9-13, doi:10.1029/2001JD000514, 2002.
- Nousiainen, T.: Optical modeling of mineral dust particles: a review, *J. Quant. Spectrosc. Ra.*, 110, 1261–1279, 2009.
- 1060 Nousiainen, T., Kahnert, M., and Veihelmann, B.: Light scattering modeling of small feldspar aerosol particles using polyhedral prisms and spheroids, *J. Quant. Spectrosc. Ra.*, 101, 471–487, 2006.
- [Scarnato, B.V., Vahidinial, S., Richard, D. T., and Kirchstetter, T. W.: Effects of internal mixing and aggregate morphology on optical properties of black carbon using a discrete dipole approximation model; \*Atmos. Chem. Phys.\*, 13, 5089–5101, doi:10.5194/acp-13-5089-2013, 2013.](#)
- 1065 [Scarnato, B.V., China, S., Nielsen, K. and Mazzoleni, C.: Perturbations of the optical properties of mineral dust particles by mixing with black carbon: a numerical simulation study, \*Atmos. Chem. Phys.\*, 15, 6913–6928, doi:10.5194/acp-15-6913-2015, 2015.](#)
- Robertson, L., Langner, J., and Engardt, M.: An Eulerian limited-area atmospheric transport model, *J. Appl. Meteorol.*, 38, 190–210, 1999.
- 1070 Saide, P. E., Carmichael, G. R., Liu, Z., Schwartz, C. S., Lin, H. C., da Silva, A. M., and Hyer, E.: Aerosol optical depth assimilation for a size-resolved sectional model: impacts of observationally constrained, multi-wavelength and fine mode retrievals on regional scale analyses and forecasts, *Atmos. Chem. Phys.*, 13, 10425–10444, doi:10.5194/acp-13-10425-2013, 2013.
- 1075 [Undén, P., Rontu, L., Järvinen, H., Lynch, P., Calvo, J., Cats, G., Cuxart, J., Eerola, K., Fortelius, C., Garcia-Moya, J. A., Jones, C., Lenderink, G., McDonald, A., McGrath, R., Navascues, B., Nielsen, N. W., Ødegaard, V., Rodriguez, E., Rummukainen, M., Rööm, R., Sattler, K., Hansen Sass, B., Savijärvi,](#)

H., Schreur, B. W., Sigg, R., The, H., and Tijm, A.: HIRLAM-5 Scientific Documentation, available at <http://www.hirlam.org/index.php/documentation> (last accessed 2016-02-15), 2002.

- 1080 Yurkin, M. A. and Hoekstra, A. G.: The discrete dipole approximation: an overview and recent developments, J. Quant. Spectrosc. Ra., 106, 558–589, 2007.